Mitochondria regulate proliferation in adult cardiac myocytes

Gregory B. Waypa, … , Edward B. Thorp, Paul T. Schumacker

Research In-Press Preview Cardiology Metabolism

Newborn mammalian cardiomyocytes quickly transition from a fetal to an adult phenotype that utilizes mitochondrial oxidative phosphorylation but loses mitotic capacity. We tested whether forced reversal of adult cardiomyocytes back to a fetal glycolytic phenotype would restore proliferative capacity. We deleted *Uqcrfs1* (mitochondrial Rieske Iron-Sulfur protein, RISP) in hearts of adult mice. As RISP protein decreased, heart mitochondrial function declined, and glucose utilization increased. Simultaneously, they underwent hyperplastic remodeling during which cardiomyocyte number doubled without cellular hypertrophy. Cellular energy supply was preserved, AMPK activation was absent, and mTOR activation was evident. In ischemic hearts with RISP deletion, new cardiomyocytes migrated into the infarcted region, suggesting the potential for therapeutic cardiac regeneration. RNA-seq revealed upregulation of genes associated with cardiac development and proliferation. Metabolomic analysis revealed a decrease in alpha-ketoglutarate (required for TET-mediated demethylation) and an increase in S-adenosylmethionine (required for methyltransferase activity). Analysis revealed an increase in methylated CpGs near gene transcriptional start sites. Genes that were both differentially expressed and differentially methylated were linked to upregulated cardiac developmental pathways. We conclude that decreased mitochondrial function and increased glucose utilization can restore mitotic capacity in adult cardiomyocytes resulting in the generation of new heart cells, potentially through the modification of substrates that regulate epigenetic modification of genes required for proliferation.

Find the latest version:

Mitochondria Regulate Proliferation
in Adult Cardiac Myocytes

Gregory B. Waypa[1,2], Kimberly A. Smith[1,2] Paul T. Mungai[1,2], Vincent J. Dudley[1,2], Kathryn A. Helmin[3], Benjamin D. Singer[3], Clara Bien Peek[4], Joseph Bass[3], Lauren Nelson[3], Sanjiv J. Shah[3], Gaston Ofman[1,2], J. Andrew Wasserstrom[3], William A. Muller[5], Alexander V. Misharin[3], G.R. Scott Budinger[3], Hiam Abdala-Valencia[3], Navdeep S. Chandel[3], Danijela Dokic[1,2], Elizabeth Bartom[4], Shuang Zhang[5], Yuki Tatekoshi[3,] Amir Mahmoodzadeh[3,] Hossein Ardehali[3], Edward B. Thorp[5] and Paul T. Schumacker[1,2,3]

Department of Pediatrics[1], Stanley Manne Children's Research Institute of the Ann and Robert H. Lurie Children's Hospital of Chicago[2], Departments of Medicine[3,] Biochemistry and Molecular Genetics[4], and Pathology[5], Northwestern University Feinberg School of Medicine Chicago, Illinois USA

Running head: Mitochondria regulate cardiomyocyte proliferation

Conflict of Interest: The authors have declared that no conflict of interest exists.

Correspondence:

Paul T. Schumacker, PhD
Department of Pediatrics
303 E. Superior St.
SMCRI 4-526
Chicago, IL 60611 USA

Ph: 312 503-1475
Email: p-schumacker@northwestern.edu

30 **Abstract**

31 Newborn mammalian cardiomyocytes quickly transition from a fetal to an adult

32 phenotype that utilizes mitochondrial oxidative phosphorylation but loses mitotic

33 capacity. We tested whether forced reversal of adult cardiomyocytes back to a fetal

34 glycolytic phenotype would restore proliferative capacity. We deleted *Uqcrfs1*

35 (mitochondrial Rieske Iron-Sulfur protein, RISP) in hearts of adult mice. As RISP protein

36 decreased, heart mitochondrial function declined, and glucose utilization increased.

37 Simultaneously, they underwent hyperplastic remodeling during which cardiomyocyte

38 number doubled without cellular hypertrophy. Cellular energy supply was preserved,

39 AMPK activation was absent, and mTOR activation was evident. In ischemic hearts

40 with RISP deletion, new cardiomyocytes migrated into the infarcted region, suggesting

41 the potential for therapeutic cardiac regeneration. RNA-seq revealed upregulation of

42 genes associated with cardiac development and proliferation. Metabolomic analysis

43 revealed a decrease in alpha-ketoglutarate (required for TET-mediated demethylation)

44 and an increase in S-adenosylmethionine (required for methyltransferase activity).

45 Analysis revealed an increase in methylated CpGs near gene transcriptional start sites.

46 Genes that were both differentially expressed and differentially methylated were linked

47 to upregulated cardiac developmental pathways. We conclude that decreased

48 mitochondrial function and increased glucose utilization can restore mitotic capacity in

49 adult cardiomyocytes resulting in the generation of new heart cells, potentially through

50 the modification of substrates that regulate epigenetic modification of genes required for

51 proliferation.

52

53 **Introduction**

54   Mitochondria generate ATP through oxidative phosphorylation (OXPHOS), but

55   they also participate in diverse biological functions that include redox signaling (1),

56   metabolite signaling (2), calcium signaling (3), and the generation of stress signals that

57   escape from the cell and act on distant tissues (4, 5). Mitochondria also play important

58   roles in synthesizing biomolecules involved in epigenetic modification of histones and

59   DNA (6). Finally, mitochondria are critical for producing substrates needed for lipid,

60   protein, and nucleotide biosynthesis, which are required for the *de novo* generation of

61   biomass in rapidly proliferating cells. In post-mitotic cells of metabolically active tissues

62   such as the heart, ATP production is considered to be the primary function of

63   mitochondria. However, the extent to which other functions of mitochondria continue to

64   contribute to cardiomyocyte function and phenotype in the mature heart is not

65   completely understood.

66   In fetal hearts where the O_2 tension is low, mitochondrial OXPHOS is minimally

67   developed, and cardiomyocytes utilize glycolysis as their principal source of energy

68   production (7, 8). Soon after birth, heart cells begin to mature by downregulating

69   glycolysis and upregulating mitochondrial biogenesis, facilitating the increase in

70   mitochondrial respiration that confers the ability in adults to sustain ATP production

71   when metabolic demand increases, as occurs during exercise. Fetal and newborn heart

72   cells are capable of undergoing mitotic cell division, but this capacity is lost soon after

73   birth, as the cells undergo the metabolic shift from glycolysis to OXPHOS (7, 9). Some

74   evidence suggests that maintenance of glycolysis may favor the retention of a

75   proliferative state (10, 11). If this shift from glycolysis to mitochondrial respiration were

76   responsible for the transition from a proliferation-competent to an adult post-mitotic state

77   in the heart (8), then it is conceivable that forcing an adult heart to shift away from

78   mitochondrial oxidative function and toward glycolysis could mimic conditions in the

79   perinatal heart and restore its proliferative capacity. However, it is widely accepted that

80   heart mitochondrial OXPHOS is essential for cardiac function and survival in adults, so

81   forcing a sudden return to glycolysis would be expected to induce lethal cardiac failure.

82   We sought to test this question by genetically disrupting mitochondrial function in adult

83   mouse hearts by deleting the *Uqcrfs1* gene which encodes the Rieske Iron-Sulfur

84   Protein (RISP), a component of complex III that is required for electron transfer and

85   proton translocation. Previous studies have shown that this gene is dispensable for cell

86   survival in other tissues and have demonstrated the importance of mitochondria for

87   functions other than ATP production (12, 13). Given the high mitochondrial density in

88   adult heart cells, we reasoned that genetic deletion of *Uqcrfs1* would cause a slow

89   transition toward glycolysis as mitochondrial turnover leads to the disappearance of the

90   pre-existing RISP protein, potentially offering ample opportunity for the cells to adjust to

91   that transition.

92   Here we report that adult mouse cardiomyocytes in which the mitochondrial

93   electron transport chain (ETC) has been diminished by RISP deletion maintain energy

94   stores, fail to develop bioenergetic stress, and continue to support mouse survival until

95   eventual depletion of RISP leads to a lethal loss of OXPHOS. Remarkably, the post-

96   mitotic cardiomyocytes returned to the cell cycle, causing the hearts to undergo growth

97   in a hyperplastic remodeling response where cellular hypertrophy, fibrosis and

98   inflammation were absent. These findings indicate that mitochondria, beyond ATP

99   production, control adult cardiomyocyte cell fate and function.

100

101 **Results**

102 **Conditional Knockout of the *Uqcrfs1* Gene Causes a Decline in Mitochondrial**
103 **Function and a Switch to Glycolysis**

104 The *Uqcrfs1* gene encodes RISP, a component of complex III required for

105 electron transfer and proton translocation. To disrupt complex III function, mice with

106 homozygous floxed alleles of *Uqcrfs1* (RISP$^{fl/fl}$) (14) were bred with heterozygous mice

107 carrying a cardiac-specific α-myosin heavy chain promoter-driven, tamoxifen-inducible

108 Cre recombinase transgene (Myh6-Cre) (15), yielding RISP$^{fl/fl}$ ± Mhy6-Cre (RISP KO

109 and RISP WT, respectively) offspring in the C57BL/6 genetic background. To assess

110 the efficacy of cardiac-specific Myh6-Cre activity, Myh6-Cre-adult mT/mG fluorescent

111 reporter mice (16) were administered tamoxifen. At 14 days post-tamoxifen, tissues

112 were analyzed for evidence of Cre-mediated conversion from constitutive expression of

113 red fluorescent protein to green. As expected, in liver where Mhy6-Cre expression is

114 absent, only the red fluorescent protein was detected (Figure 1A). By contrast,

115 following Cre activation, heart cells uniformly demonstrated green fluorescence; the only

116 cells still exhibiting red fluorescence were capillaries and coronary blood vessels,

117 indicating high efficiency of in vivo recombination in adult cardiomyocytes. Next, RISP

118 WT and KO mice received tamoxifen between 5-7 weeks of age; levels of residual RISP

119 protein in the heart were assessed at 30, 60 and 75 days thereafter (Figure 1B). RISP

120 protein in heart lysates was significantly decreased at 30 days; by 60 days the protein

121 was >90% depleted and by 75 days was minimally detectable in RISP KO, compared

122 with RISP WT (Figure 1C,D). Loss of RISP disrupts complex III of the ETC and

123 abolishes OXPHOS by preventing electrons generated at complex I or II from reaching

124 cytochrome c oxidase (complex IV). To assess the expected decline in mitochondrial

125   function, hearts were rapidly harvested at 60 days and respiration was measured in

126   isolated mitochondria (Supplemental Figure S1A). These studies revealed a significant

127   but incomplete decrease in rotenone-inhibited, succinate-driven respiration by complex

128   III in the RISP KO mice. However, absolute respiration at complex IV was not different

129   when electrons were delivered directly to cytochrome c (thus bypassing complex III),

130   indicating that the decline in function was limited to complex III. In mitochondria from

131   75-day hearts, respiration at complex III relative to complex IV was nearly abolished

132   (Supplemental Figure S1B). In cells lacking a functional ETC, mitochondrial inner

133   membrane potential ($\Delta\Psi$m) is sustained by mitochondrial ATP synthase, which operates

134   in reverse by taking up ATP derived from cytosolic glycolysis or substrate-level

135   phosphorylation. Hydrolysis of that ATP in the matrix by complex V allows the ATP

136   synthase to operate in reverse, sustaining $\Delta\Psi$m by extruding protons across the inner

137   membrane (17). To assess the consequences of RISP depletion on mitochondrial

138   potential, neonatal cardiomyocytes were isolated from RISP^{fl/fl} mice carrying

139   constitutively active Cre under the control of the muscle creatine kinase promoter (MCK)

140   and maintained in tissue culture for >14 days. Both RISP WT and KO cells exhibited

141   polarized mitochondria. However, myxothiazol (2 μM) which inhibits complex III, caused

142   a greater decrease in $\Delta\Psi$m in WT cells, indicating that forward flux in the ETC was

143   contributing to the maintenance of mitochondrial polarization. By contrast, RISP-

144   deficient cells were better able to maintain potential during myxothiazol treatment,

145   indicating that the ETC was not contributing to the maintenance of $\Delta\Psi$m in cells

146   depleted of RISP (Supplemental Figure S1C). RISP WT cardiomyocytes survived in 15

147   mM galactose (without glucose), whereas RISP KO cardiomyocytes detached from

148   coverslips in galactose medium, confirming a dependence on glycolytic metabolism in

149   those cells (data not shown). These results demonstrate that progressive loss of RISP

150   in adult mouse cardiomyocytes leads to a decline in mitochondrial function, forcing a

151   switch toward glycolysis. At 60 days after tamoxifen the ETC still retains partial

152   function, but by 75 days a virtually complete loss of RISP forces a condition where the

153   cells must rely on glycolysis for survival.

154   The partial decline in complex III function in 60 day RISP KO hearts was

155   associated with increased cardiac glucose utilization, as assessed by ^{18}F-

156   fluordeoxyglucose utilization measured by positron emission tomography (FDG-PET)

157   (Figure 1E,F,G, Supplemental Figure S1D). This was associated with a decrease in

158   ATP concentration in rapidly frozen hearts (Figure 1H). However, there was no

159   indication of bioenergetic deficiency, as the adenylate energy charge

160   (([ATP]+0.5[ADP])/([ATP]+[ADP]+[AMP]) was not diminished (Figure 1I, Supplemental

161   Figure S1E). More convincingly, AMP kinase (AMPK), a master sensor of cellular

162   energy stores and regulator of energy usage (18) was not activated in 60-day control or

163   RISP KO hearts, as indicated by its lack of phosphorylation. By contrast, even brief

164   ischemia during rapid heart harvest resulted in its phosphorylation and thus activation

165   (Figure 1J,K). Thus, 60-day RISP KO hearts show a partial decline in ETC function and

166   an accompanying increase in glucose utilization without evidence of bioenergetic crisis.

167   **RISP Depletion in Cardiomyocytes Induces Cardiomegaly without Affecting**
168   **Cardiomyocyte Size or Ultrastructure**

169   Hearts from RISP KO mice exhibited a remarkable increase in size compared to

170   RISP WT littermates (Figure 2A). Cardiac remodeling was not evident at 30 days when

171   RISP protein was still abundant, but by 60 days when RISP was significantly decreased

172   the heart weight/body weight ratios (HW/BW) had more than doubled (Figure 2B) while

173   body weights did not differ (Supplemental Figure S2A). Left ventricular (LV) weight also

174   increased progressively between the 30- and 60-day time points, but less so between

175   60 and 75 days (Figure 2C). Mice began to die after approximately 75 days, possibly as

176   a consequence of severe loss of OXPHOS as evidenced by earlier experiments

177   (Supplemental Figure S1B). While cursory examination suggested that the LV changes

178   were reminiscent of the remodeling response to pressure overload, (19) parallel

179   changes were seen in LV and right ventricle (RV)+Septum weights, indicating that

180   remodeling encompassed the entire heart (Supplemental Figure S2B). Moreover, mean

181   systemic arterial blood pressure was modestly decreased in awake RISP KO compared

182   with RISP WT mice (Supplemental Figure S2C). Importantly, histological comparison

183   between RISP KO and RISP WT even at 75 days revealed that despite the extensive

184   cardiomegaly, no differences in cell morphology were evident (Figure 2D).

185   Inflammatory cell infiltration was absent, and no fibrotic remodeling (Masson's trichrome

186   staining) was detected (Figure 2E). To quantify cell size, heart sections were subjected

187   to periodic acid-Schiff (PAS) staining to identify cell margins, and cell widths across the

188   LV wall were assessed employing an unbiased image analysis process using ImageJ.

189   Although LV wall thickness was modestly increased (Supplemental Figure S3A),

190   cardiomyocyte width was not different from controls (Supplemental Figure S3B),

191   indicating an absence of cardiomyocyte hypertrophy. Moreover, cell counts across the

192   LV wall were not increased (Supplemental Figure S3C). To further assess remodeling,

193   wheat germ agglutinin staining was carried out (Supplemental Figure S3D,E) and

194   individual cell cross-sectional areas were measured in heart sections. Again, no

195 difference in cell cross-sectional area between RISP KO and WT heart cells was

196 detected, indicating an absence of hypertrophic remodeling (Supplemental Figure S3F).

197 Counts of capillaries in the LV wall did increase (Supplemental Figure S3G). Contractile

198 fiber ultrastructure (Supplemental Figure S4A), mitochondrial ultrastructure

199 (Supplemental Figure S4B), and mitochondrial abundance (Supplemental Figure S4C),

200 assessed by electron microscopy, were indistinguishable between WT and KO hearts.

201 Collectively these data indicate that partial disruption of the mitochondrial ETC causes

202 remodeling involving dramatic cardiomegaly, with increases in heart size but no change

203 in cardiomyocyte size or ultrastructure.

204 **RISP Depletion Causes Hyperplastic Remodeling of the Heart and an Activation of**
205 **Cardiomyocyte Proliferation**

206   These results suggested that the decline in ETC function and the increase in

207 glycolysis is associated with a return of cardiomyocyte proliferation. To assess this,

208 heart sections were co-stained for Ki-67, a nuclear marker of proliferation and myosin

209 light chain, a cardiomyocyte marker (Figure 2F). No difference from wild type was

210 detected at 30 days, but by 60 days there was clear evidence of proliferation in the

211 RISP KO cardiomyocytes (Figure 2G). Notably, evidence of cardiomyocyte proliferation

212 was relatively abundant at 60 days but absent by 75 days. A similar pattern indicating

213 increased mitosis in co-stained cardiomyocytes was seen with phospho-histone H3

214 nuclear staining (Figure 2H, Supplemental Figure S4D). Finally, to confirm those results,

215 RISP KO and WT mice were administered 5-ethyny-2'-deoxyuridine (EdU) by

216 subcutaneous micro-osmotic pump between 30 and 60 days; these studies revealed

217 evidence of cardiomyocyte DNA synthesis, indicating that proliferation had been

218 activated (Figure 2I). These results indicated that evidence of cardiomyocyte

219   proliferation develops by 60 days, but later halts in association with the development of

220   severe ETC deficiency.

221   While the above findings support the conclusion that cardiomyocyte proliferation

222   was activated, a more rigorous test requires quantification of cell numbers. To

223   genetically identify cardiomyocytes, mT/mG fluorescent reporter mice (16) were bred

224   with RISP KO and RISP WT mice. Adult mice received tamoxifen to label the

225   cardiomyocytes with green fluorescence and, in the fl/fl mice, to delete RISP. Hearts

226   were harvested after 60 days, fixed, and digested to compare cell numbers and

227   cardiomyocyte dimensions (Figure 3A). Cardiomyocytes were distinguished from other

228   cell types by their rod-shaped appearance and green fluorescence. No differences in

229   cell length (Figure 3B) or width (Figure 3C) were detected, confirming the absence of

230   hypertrophy as evidenced by earlier experiments (Figure 2E, Supplemental Figure

231   S3B,D,E,F). However, the number of cardiomyocytes from the RISP KO hearts

232   increased from nearly 500,000 to approximately 1 million, confirming the presence of

233   hyperplastic remodeling (Figure 3D). DAPI co-staining was used to quantify the number

234   of nuclei per cell; this revealed an increase in the number of mononuclear and a

235   decrease in the number of diploid cardiomyocytes in the RISP KO mice compared to

236   controls (Figure 3E). Thus, some of the new cells likely arose from cell division of

237   binuclear cardiomyocytes in the heart. Consistent with the increased cardiomyocyte

238   numbers, the total number of cardiomyocyte nuclei, as well as the number of

239   mononuclear cardiomyocyte nuclei, increased in the RISP KO hearts (Figure 3F). Thus,

240   the proliferation of cardiomyocytes involved the division of existing binuclear into

241   mononuclear cells, as well as de novo synthesis of new mononuclear cardiomyocytes,

242 also evidenced by the increase in EdU-positive nuclei (Figure 2I). How could the

243 number of cells in the heart have doubled when the number of cells across the LV wall

244 did not change? We propose that cell division occurred along the long axis of the

245 cardiomyocytes (end-to-end division) and that subsequent growth in the length of the

246 daughter cells produced an increase in the circumferential dimension of the ventricular

247 wall without increasing its lateral dimension (Figure 3G). This produced a dramatic

248 increase in the size of the heart characterized by an enlarged ventricular chamber, a

249 slight increase in LV wall thickness and no evidence of cellular hypertrophy.

250   Echocardiography assessments in anesthetized mice revealed a progressive

251 decrease in LV fractional shortening (Figure 4A) and LV ejection fraction (Figure 4B).

252 Both LV end-diastolic (Figure 4C) and end-systolic diameters (Figure 4D) were

253 increased. However, heart rate and stroke volume were maintained (Figure 4E,F), so

254 the calculated cardiac output was preserved (Figure 4G). Hematocrit was unaffected

255 (Figure 4H). Thus, RISP KO hearts continue to function with a partial loss of ETC

256 function, although the decline in diastolic and systolic function became severe by 75

257 days.

258 **RISP KO-Mediated Cardiomyocyte Proliferation Induces Heart Regeneration in**
259 **Regions of Ischemic Injury**

260   Can new cardiomyocytes repair myocardium damaged by ischemia? To test

261 this, initial experiments were carried out to determine whether ischemia produces an

262 equivalent extent of injury in RISP KO and WT hearts. Hearts at 45 days were

263 subjected to ischemia and reperfusion of the coronary artery to induce ischemic injury.

264 After 48 hrs, hearts were harvested and the area of ischemia (infarct size) relative to the

265 area at risk was quantified (Supplemental Figure S5A,B,C). These studies revealed

266 equivalent injury in both groups, indicating that RISP KO does not affect the extent of

267 ischemic injury at that time point (Supplemental Figure S5D). Next, control and RISP

268 KO hearts were subjected to ligation of a distal segment of the coronary artery at 45

269 days and were harvested for analysis at 60 days. Cardiomyocyte division had

270 previously been shown to be active between 45 and 60 days, so we sought to

271 determine whether new cells generated during that period would migrate into the region

272 of previous ischemic injury. Clear evidence of ischemic injury was observed in these

273 hearts (Figure 5A,D). The periphery of the injured area was outlined using ImageJ

274 (Figure 5B,E), and an ellipse with an equivalent area was generated (Figure 5C,F). The

275 ratio of the circumference of the ellipse to the circumference of the ischemic area was

276 then calculated to provide an index of the irregularity in the periphery of the scar region

277 for the two groups. Visual inspection revealed that projections of live cardiomyocytes

278 were penetrating the injured area in the RISP KO hearts, giving rise to the jagged and

279 irregular periphery of the injured area summarized in Figure 5G. By contrast, the

280 control hearts demonstrated a smoother and more confluent boundary to the injured

281 area. Ischemic injury had no effect on the increase in HW/BW differences (Figure 5H).

282 Cardiac function in the RISP KO hearts was significantly impaired compared to wild type

283 hearts; that impairment was large compared to the effect of myocardial ischemia in wild

284 type controls (Figure 5I,J). However, the severity of infarction was not sufficient by itself

285 to decrease cardiac function. A less severe infarction was used in order to minimize

286 lethality during the 48 hour post-operative period. As the new cells generated in the

287 RISP KO hearts were functionally impaired, they were unable to restore cardiac

288 performance in the ischemic hearts. These findings reveal that newly formed

289 cardiomyocytes have the potential to migrate into an area of the heart that has

290 sustained ischemic injury. While this did not appear to reduce the fibrotic remodeling in

291 the injured area, the proliferative response involves new cardiomyocytes re-populating

292 heart regions damaged by ischemia.

293 **Hyperplastic Remodeling of the Heart Involves Cardiomyocyte Proliferation**

294   To determine the lineage of new cells in the heart, mT/mG-RISP KO and WT

295 mice were generated (16). Adult mouse hearts were analyzed 60 days after tamoxifen

296 (Supplemental Figure S6A). If non-myocyte progenitor cells had migrated from bone

297 marrow to the heart and differentiated into cardiomyocytes, these new cells would have

298 displayed red fluorescence because the Myh6-Cre is only expressed in differentiated

299 heart cells. Analysis revealed no red fluorescent cardiomyocytes in RISP KO hearts,

300 and only red fluorescence in the mT/mG-RISP WT hearts. Flow cytometry analysis of

301 bone marrow from RISP KO reporter mice revealed only red fluorescent cells, indicating

302 that Myh6-Cre-positive cells are absent in bone marrow (Supplemental Figure S6B-D).

303 Hence, the new heart cells must have originated from existing cardiomyocytes rather

304 than from migrating progenitors.

305 **RISP KO-Mediated Cardiomyocyte Proliferation Involves mTOR Activation but is**
306 **Not Caused by Decreased ROS Signaling or Meis 1 Levels.**

307   The mitochondrial ETC generates reactive oxygen species (ROS), which could

308 cause oxidative DNA damage and trigger cell-cycle arrest (20). RISP KO decreases

309 ROS generation at complex III (21). A decrease in ROS-induced DNA damage might

310 therefore allow cardiomyocytes to return to the cell cycle. To determine the

311 consequences of RISP KO on ROS generation, subcellular thiol oxidant status was

312 assessed in neonatal cardiomyocytes from RISP$^{fl/fl}$-creatine kinase Cre mice using the

14

313 genetically encoded redox sensor, roGFP, expressed in the cytosol or mitochondrial

314 matrix (22). RISP KO cells exhibited a significant decrease in mitochondrial thiol

315 oxidation, consistent with the loss of ROS from complex III (Supplemental Figure S7A).

316 By contrast, cytosolic oxidant status was unchanged. To assess the effect of RISP

317 deletion on nuclear DNA oxidation, 8-oxo-deoxyguanine (8-oxo-dG) immunostaining in

318 cardiomyocyte nuclei was assessed in adult RISP WT and KO mice at 60 days post-

319 tamoxifen (Supplemental Figure S7B). Nuclear 8-oxo-dG staining was decreased in

320 RISP KO heart cells, compared to controls (Supplemental Figure S7C). Does this

321 decrease in DNA damage enable cardiomyocytes to re-enter the cell cycle? To test

322 this, oxidant stress was restored in RISP KO mice by placing them on a diet containing

323 menadione (2-methyl-1,4-naphthoquinone, 120 mg·kg^{-1}·day^{-1}), a redox-cycling vitamin

324 K precursor shown previously to induce systemic oxidant stress (23). In other mice,

325 menadione was supplemented with ascorbic acid (120 mg·kg^{-1}·day^{-1}) to enhance the

326 redox cycling rate (24); this combination was previously shown to confer therapeutic

327 benefit in a patient with a partial loss-of-function mutation in complex III (25, 26). The

328 menadione diet began at 30 days after tamoxifen administration and continued until day

329 60, the period during which cardiac remodeling occurs after RISP KO. Hearts were

330 then harvested and assessed for 8-oxo-dG staining in cardiomyocyte nuclei and for

331 cardiac remodeling. The decrease in nuclear oxidant stress in RISP KO hearts was

332 reversed in the mice treated with menadione (Supplemental Figure S7C). However,

333 significant increases in HW/BW were still observed in the RISP-deficient hearts

334 (Supplemental Figure S7D). Nuclear staining for Ki-67 (Supplemental Figure S7E,F)

335 and phospho-histone H3 was still indistinguishable between RISP-deficient control-fed

336 and menadione-fed, mice, at 60 days (Supplemental Figure S7G). Total adenine

337 nucleotide levels decreased in the RISP-deficient hearts, but these were not restored by

338 menadione-ascorbate treatment (Supplemental Figure S7H,I). Finally, cardiac

339 performance as assessed by echocardiography was not affected by menadione

340 treatment (Supplemental Figure S7J,K,L). Collectively, these data indicate that

341 decreased ROS signaling from mitochondria is not responsible for the proliferative

342 response in the adult RISP KO hearts.

343 Remodeling in RISP KO hearts is likely driven by a change in transcription of

344 genes regulating growth and differentiation. Previously, the transcription factor, Meis1,

345 was shown to increase in neonatal hearts as the cardiomyocytes transitioned to a state

346 of proliferative arrest (27). Moreover, deletion of Meis1 in neonatal mouse

347 cardiomyocytes extended the postnatal proliferative window. However, we did not

348 detect a decrease in the mRNA message for Meis1 or protein expression in the RISP

349 KO hearts, suggesting that Meis1 is not responsible for the remodeling we observed

350 (Supplemental Figure S8A,B).

351 The kinase mTOR is a nutrient sensor that functions as a master regulator of cell

352 growth and proliferation (28). Proliferating cardiomyocytes would be expected to exhibit

353 mTOR activation, as its phosphorylation of protein targets regulates mRNA translation

354 in accordance with amino acid and glucose availability (29). Ribosomal S6 protein is

355 one such target, and RISP KO hearts at 60 days exhibited robust phosphorylation and

356 activation (Figure 6A,B). Phosphorylation of S6 is mediated by S6 Kinase, which also

357 exhibited significant activation in RISP KO hearts (Figure 6C,D). Growth factor

358 signaling leads to the phosphorylation and activation of the phosphatidylinositol-3-

359   kinase, Akt, a positive regulator of mTOR. In RISP KO hearts we observed increased

360   Akt phosphorylation (pAkt) compared with WT (Figure 6E,F), suggesting that the

361   activation of growth factor signaling contributed to the upregulation of mTOR signaling

362   in RISP KO hearts. Activation of AMPK in response to bioenergetic deficiency would

363   lead to rapid inhibition of mTORC1 (30), so the increased mTOR activity is consistent

364   with our observed activation of cardiomyocyte proliferation and absence of bioenergetic

365   deficiency, as described in earlier experiments (Figure 1J,K).

366   **RISP Depletion Mediates a Transcriptional Response Consistent with an**
367   **Upregulation of Heart Developmental Processes**

368   To explore the transcriptional response, RNA-seq was performed on RNA

369   collected from rapidly frozen tissue harvested from RISP KO and WT adult mice. RISP

370   KO hearts at 60 days revealed an up- or down-regulation of 1355 genes (FDR adjusted

371   p<.05) compared to controls (Figure 7A,B). As expected, expression of *Uqcrfs1* was

372   decreased (adj. p<1.44E-39, log2 fold-change -4.44). Changes were also detected in

373   genes linked to the mitochondrial unfolded protein response and the amino acid

374   starvation response (Table 1). For example, significant upregulation of activating

375   transcription factors *Atf3*, *Atf4* and *Atf5*, fibroblast growth factor 21 (*Fgf21*), growth

376   differentiation factor 15 (*Gdf15*) and methylene tetrahydrofolate dehydrogenase, the

377   rate-limiting enzyme in the folate cycle of mitochondria, were noted. In the RISP KO

378   hearts, gene ontology (GO) analysis of biological processes revealed significant

379   upregulation of multiple pathways related to the observed remodeling, including

380   cardiovascular system development, vascular development, cell proliferation and other

381   developmental processes, consistent with the concept that RISP deletion causes a

382   reawakening of developmental processes (Table 2). Downregulated biological

383   processes were linked to regulation of cardiac muscle contraction, heart contraction and

384   regulation of heart rate, consistent with the impaired contractile ability in the knockout

385   hearts (Table 3).

386   Consistent with the evidence of mTOR activation, a number of growth factor

387   genes were significantly altered as well, with insulin-like growth factor 1 (*Igf1*), heparin-

388   binding EGF-like growth factor (*Hbegr*), and connective tissue growth factor (*Ctgf*)

389   showing significant increases (Table 4). No increase in *Vegfa*, *b* or c was detected,

390   although interestingly the remodeling was associated with an increase in capillary

391   density (Supplemental Figure S3G). These results reveal that RISP KO leads to a

392   transcriptional response consistent with an upregulation of developmental processes in

393   the heart, which aligns with the observed hyperplastic phenotype.

394   To clarify the mechanism responsible for the decline in cardiac function

395   described earlier (Figure 4), we assessed Ca^{2+} activation in freshly isolated electrically

396   paced adult cardiac myocytes from RISP KO and WT hearts loaded with Rhod-4AM at

397   60 days post-tamoxifen. No differences were detected in the rising phase of activation,

398   or in the peak levels of Ca^{2+} (Figure 8A and Supplemental Figure S9A-H). However, the

399   rate of decline in Ca^{2+} was significantly faster in the RISP KO cells compared to

400   controls. The faster sequestration of Ca^{2+} is characteristic of younger hearts, consistent

401   with the proposed upregulation of developmental processes in the RISP-deficient

402   hearts. Moreover, as Ca^{2+} uptake is an energy-dependent process, this response is

403   consistent with the absence of bioenergetic stress.

404   The observation that calcium activation was normal in RISP KO cells indicated

405   that the cardiac functional defect must be downstream from Ca^{2+} signaling. The

18

406   transcriptional analysis had identified downregulation of gene sets linked to regulation of

407   cardiac muscle contraction. Notably, expression of myosin light chain kinase 3 (*Mylk3*),

408   which is critical for sustaining contractile function, was significantly downregulated at the

409   mRNA level. Western blot analysis confirmed that protein expression was also

410   decreased in the RISP KO hearts (Figure 8B,C). These findings suggest that

411   decreases in expression of proteins sustaining cardiac contractility likely contributed to

412   the decline in cardiac function, although other factors downstream from calcium

413   signaling could also have contributed.

414   Although Hippo-YAP/TAZ signaling has been implicated in organ regeneration

415   (31), western blotting of phospho-YAP relative to total YAP protein demonstrated no

416   difference between wild type and RISP KO hearts (data not shown).

417   **RISP KO Results in Alterations of Metabolic Substrate Levels Which Alter DNA**
418   **Methylation and Gene Expression**

419   Why would loss of complex III trigger a transcriptomic response leading to

420   cellular hyperplasia? As mitochondria are critical for diverse metabolic functions in the

421   cell, one possibility is that progressive ETC loss alters cellular metabolite levels that

422   contribute to growth, cell proliferation and the regulation of gene transcription. To

423   explore this, hearts of anesthetized, mechanically ventilated RISP KO and WT control

424   mice were snap frozen in situ and analyzed for metabolite levels by LC-Mass

425   spectrometry of 695 known biochemicals. A total of 298 biochemicals were significantly

426   altered (190 increased, 108 decreased) in the RISP KO hearts. Principal component

427   analysis detected significant distinction between WT and RISP KO hearts

428   (Supplemental Figure S10A). Random Forest classification revealed key differences in

429   lipid, amino acid and carbohydrate metabolism compared with wild type hearts

430   (Supplemental Figure S10B). Consistent with the loss of ETC function, significant

431   increases in glycolytic intermediates were detected, including glucose, glucose-1,6-

432   diphosphate, fructose 1,6-diphosphate, dihydroxyacetone phosphate, 3-

433   phosphoglycerate, phosphoenolpyruvate, pyruvate, and lactate (Figure 9A). In the

434   pentose phosphate pathway, 6-phosphogluconate was increased, although ribose-1-

435   phosphate was decreased. Similarly, fructose, mannitol/sorbitol and mannose were

436   significantly elevated in RISP KO hearts compared to controls. By contrast,

437   components of the Krebs cycle were significantly diminished, including oxaloacetate,

438   citrate, aconitase, alpha-ketoglutarate, and succinate. Fumarate and malate were

439   significantly increased. Membrane remodeling pathways were also affected, with

440   decreases in choline, CDP-choline, and CDP-ethanolamine, but increases in

441   phosphatidylcholine and phosphatidylethanolamine (Figure 9B). Increases in polyamine

442   synthesis have been linked to increases in proliferation, while decreases have been

443   noted in senescent cells (32). In RISP-deficient hearts, polyamine metabolism was

444   significantly affected, with increases in putrescine, spermidine, N^1-acetylspermidine,

445   and 5-methylthioadenosine (MTA) (Figure 9C). Finally, increases were detected in fatty

446   acid metabolism intermediates and acyl carnitine, along with, hexanoyl, palmitoyl,

447   linoleoyl, oleoyl, myristoleoyl and arachidoyl carnitines (Figure 9D), which may

448   represent a backup of mitochondrial fatty acid β-oxidation caused by limitations in the

449   ETC. These findings reveal that RISP KO causes a shift in metabolism that leads to

450   alterations in metabolite levels, which could conceivably drive the transcriptional

451   response.

452   How could altered metabolite levels affect transcription? Gene expression is

453 affected by chromatin structure, and DNA methylation at cytosines of the nucleotide

454 sequence CpG is a key mechanism in the epigenetic regulation of gene expression.

455 One important mitochondrial task is to supply substrates used by enzymes involved in

456 DNA methylation/demethylation. For example, alpha-ketoglutarate, a Krebs cycle

457 intermediate, is a required substrate for DNA demethylation by the TET family of

458 dioxygenases, while S-adenosylmethionine (SAM) is the methyl donor for DNA

459 methyltransferases (33). Alterations in the availability of these substrates after RISP

460 deletion could therefore alter epigenetic regulation of transcription. Inhibition of the ETC

461 can also increase the production of L-2-hydroxyglutarate (2-HG), a competitive inhibitor

462 of demethylases, via promiscuous reduction of alpha-ketoglutarate by malate

463 dehydrogenase (MDH) or lactate dehydrogenase (LDH) (34, 35). Moreover, in the

464 absence of complex III function, the conversion of 2-HG back to alpha-ketoglutarate by

465 2-HG dehydrogenase is inhibited (12, 13). Succinate and fumarate can also inhibit

466 demethylase activities (6). To assess metabolite levels affecting

467 methylation/demethylation, the ratios of 2-HG/alpha-ketoglutarate, succinate/ alpha-

468 ketoglutarate, and fumarate/alpha-ketoglutarate were compared in RISP-deficient and

469 control hearts (Figure 9E). These ratios increased, as did the ratio of SAM to S-

470 adenosylhomocysteine (SAH), favoring an increase in methylation. Thus, the observed

471 changes in metabolite levels could conceivably alter DNA methylation in the RISP KO

472 mice, thereby inducing transcriptional changes that drive developmental processes and

473 cell proliferation.

474   To determine the effects of RISP KO on CpG methylation, DNA methylation

475   profiling was assessed using a modified reduced-representation bisulfite sequencing

476   method to identify the CpG methylation landscape responses in snap-frozen hearts (36-

477   40). This identified 4,558 differentially methylated CpG sites (FDR≤.05) with a significant

478   global increase in DNA methylation across the genome (Figure 10A). Of these, 1104

479   differentially methylated CpGs were most likely to affect translation, as they were

480   located within 2 kb of the transcriptional start sites of genes (Figure 10B). Comparison

481   of genes that were both differentially expressed (DEG) and differentially methylated

482   (DMC) revealed 115 common elements. This overlapping gene set was linked to

483   relevant upregulated pathways related to the observed RISP KO heart phenotype

484   including cardiac muscle tissue development, heart development, muscle cell

485   development, muscle structure development, myofibril assembly, striated muscle cell

486   differentiation, and sarcomere organization (Table 5). In addition, significant

487   downregulation of other processes were identified in the GO analysis of overlapping

488   genes (Table 6), some of which were linked to regulation of cardiac muscle contraction,

489   heart contraction and regulation of heart rate, again consistent with the impaired

490   contractile ability in the knockout hearts. K-means clustering of these genes revealed a

491   data structure similar to the k-means clustering of all differentially expressed genes in

492   Figure 7B (Figure 10C). Of these 115 genes, 93 passed a stringent DNA methylation

493   filter designed to detect genes with promoters bearing CpG methylation that is anti-

494   correlated with their expression (36) (Figure 10D). A comparison between the change in

495   expression (increased vs. decreased) and methylation status revealed that the majority

496   of suppressed genes had undergone an increase in methylation, whereas those

497   showing an increased expression in the RISP KO demonstrated a decrease in

498   methylation (Figure 10E). Why did methylation decrease for certain genes when overall

499   CpG methylation increased? Most likely, the increased methylation caused by

500   metabolomic changes altered the expression of genes having secondary effects on

501   methylation, resulting in a mixture of genes with increased or decreased methylation

502   and decreased or increased expression, respectively.

503   Pathway analysis revealed that these differentially expressed and methylated

504   genes were associated with upregulated developmental processes including muscle

505   structure development, cardiac muscle development and cell development. The list of

506   specific genes that were differentially methylated and differentially expressed (Table 7),

507   however, have not previously been linked to cell proliferation. These findings reveal

508   that RISP KO alters the availability of substrates affecting DNA methylation, resulting in

509   changes in methylation of CpGs in the promoter regions of genes broadly linked to

510   cardiovascular development. Moreover, changes in the expression of these genes

511   corresponded to the changes in the methylation status of their promoters.

512   To address the possibility that Myh6-Cre activation in wild type mice might affect

513   cardiac remodeling or function, we compared HW/BW and cardiac function in Cre-

514   negative and Cre-positive RISP$^{+/+}$ mice at 60 days post-tamoxifen (Supplemental Figure

515   S12A-F). No differences were observed, indicating that Cre activation by itself does not

516   induce cardiac remodeling or changes in cardiac function.

517

518 **Discussion**

519   Genetic deletion of *Uqcrfs1* in adult cardiomyocytes leads to a progressive loss

520 of RISP protein in the heart. At the point where partial inhibition of mitochondrial

521 function has developed, these hearts demonstrate an upregulation of glycolysis, as

522 indicated by ^{18}F-FDG-PET scanning and increased tissue lactate and pyruvate levels.

523 As the decline in ETC function progresses, the hearts undergo profound hyperplastic

524 remodeling and develop a progressive cardiomegaly, as evidenced by increased

525 nuclear staining for Ki-67 and phospho-histone H3, increases in EdU staining in vivo, a

526 doubling of the number of cardiomyocytes by direct counting of digested hearts, and a

527 parallel increase in the total number of cardiomyocyte nuclei. The loss of RISP is

528 associated with an upregulation of transcriptional pathways associated with heart and

529 cardiovascular development as well as cell proliferation, but a downregulation of

530 pathways associated with contractile function. Collectively, these findings are

531 consistent with the conclusion that RISP deletion in the heart induces de-differentiation

532 toward a perinatal developmental state, with increased glycolysis and a restoration of

533 mitotic capacity but a decrease in contractile function.

534   A bioenergetic crisis was not induced by RISP KO, as evidenced by (a) lack of a

535 decrease in cellular energy charge, (b) absence of AMPK activation, (c) evidence of

536 mTOR and Akt activation that is consistent with the proliferative response but

537 inconsistent with a bioenergetic deficiency (29), and (d) sustained peak Ca^{2+} activation,

538 and accelerated Ca^{2+} sequestration resembling the behavior of younger heart cells.

539 The data also suggest that shifts in cardiac metabolism arising from RISP depletion led

540 to increases in metabolite levels that promote DNA methylation and decreases in alpha-

541   ketoglutarate needed for demethylation, resulting in increased in CpG methylation within

542   regulatory regions of genes that promote cardiac development. Thus, by regulating

543   cellular metabolism affecting epigenetic control, mitochondria regulate developmental

544   state and mitotic capacity in cardiomyocytes. It is conceivable that the normal

545   developmental progression from fetal glycolytic metabolism toward the mitochondrial

546   OXPHOS in the postnatal heart contributes to the loss of proliferative capacity that

547   persists through adulthood.

548   Mitochondrial cardiomyopathies arising from complex III dysfunction have been

549   linked to hypertrophic remodeling, which can progress to decompensation and dilation

550   of the left ventricle (41). However, we detected no similarities to cardiac hypertrophy or

551   dilated cardiomyopathy in terms of the DEGs. In that regard, a comparison between a

552   set of 35 DEGs identified in hypertrophic hearts (42) with our top 275 DEGs identified

553   zero overlap. We also compared our top 275 DEGs to the top 50 genes distilled from

554   multiple RNA seq studies of dilated cardiomyopathy (43). This, too, revealed no

555   overlap. Thus, the gene signatures of the RISP KO hearts don't resemble those of

556   hypertrophic or dilated cardiomyopathy.

557   The cellular morphology and cardiac structure also failed to resemble a classical

558   hypertrophic or dilated cardiomyopathy. In hypertrophic hearts an increase in the lateral

559   cell dimension would be expected, but RISP KO cardiomyocyte dimensions at 60 days

560   were indistinguishable from controls. Dilated cardiomyopathies are characterized by

561   increased LV volume, a thinned LV wall and likely with a decrease in cell width. The

562   RISP-deleted hearts did have increased LV volumes, but the LV wall was only slightly

563   thickened, the widths of the cells were unaffected, and the total number of

564 cardiomyocytes had doubled. This picture is consistent with end-to-end cell division

565 and subsequent growth leading to a large increase in LV circumference without a

566 change in the number of cells across the LV wall or a change in cell dimensions (shown

567 schematically in Figure 3G). In that sense, comparisons between the RISP KO

568 phenotype and a classical dilated heart should be made with caution.

569   The increase in HW/BW was associated with a small but significant increase in

570 posterior wall thickness (PWT) and an increase in LV end-diastolic volume (LVEDV) as

571 assessed by echocardiography (Supplemental Figure S11A,B). However, there was no

572 change in LVEDV/PWT (Supplemental Figure S11C) and no increase in LVEDV/HW

573 (Supplemental Figure S11D), as would be expected for a dilated heart. Hence, the

574 increased size of the LV is not out-of-proportion to the larger heart weight – these are

575 larger hearts by virtue of having twice the number of cardiomyocytes versus controls.

576 The larger LV chambers are not disproportionate to the increased heart size.

577 Collectively, these data indicate that the remodeling produces a larger heart with

578 chamber sizes that are consistent with the larger heart mass. Hence, the RISP hearts

579 resemble neither a dilated cardiomyopathy nor hypertrophic remodeling. The ratio of

580 binuclear/mononuclear cells decreased during remodeling, so some of the new

581 cardiomyocytes were the product of binuclear cells dividing into mononuclear, a process

582 that would naturally slow as the binuclear pool of cardiomyocytes decreased. However,

583 the total number of cardiomyocyte nuclei increased in parallel with the number of

584 cardiomyocytes, so de novo cardiomyocyte synthesis also contributed. To our

585 knowledge this remodeling process has not been described previously.

586   If a bioenergetic deficiency did not exist, why was contractile function impaired?

587   Studies of peak Ca^{2+} activation in paced cells revealed no differences between RISP

588   KO and control cardiomyocytes, suggesting that the mechanism must lie downstream

589   from calcium activation. The transcriptional GO analysis revealed a downregulation of

590   genes linked to contractile function, including *Mylk3* which phosphorylates myosin light

591   and heavy chains, thereby potentiating the force and rate of cross-bridge recruitment in

592   cardiac myocytes (44). Interestingly, this gene was also among the cohort of

593   differentially methylated and differentially expressed genes. Western blotting revealed

594   that its protein expression at 60 days was suppressed, consistent with the idea that

595   these cells have "walked back" developmentally toward a perinatal stage that lacks the

596   contractile activity normally seen in adult cardiomyocytes.

597   Expression of multiple growth factor genes was increased after RISP KO (Table

598   1), which likely contributed to the increased Akt phosphorylation and mTOR activation in

599   60-day hearts. The role of mTOR in the regulation of aerobic glycolysis is complex and

600   not fully understood (45). However, it is conceivable that the increase in glycolytic flux

601   we observed, in the absence of transcriptional activation of glycolytic genes, could have

602   been facilitated by mTOR through its ability to upregulate glucose transporters to the

603   plasma membrane of cardiomyocytes (46).

604   Previous reports have linked specific genes to the cell cycle arrest in

605   cardiomyocytes. Meis1 was reported to control cell cycle arrest in hearts of newborn

606   mice, and genetic deletion of Meis1 and its cofactor Hoxb13 was shown to activate

607   mitosis in adult mouse hearts (27, 47). However, we found no changes in message or

608   protein levels of Meis1 in the RSIP KO hearts, indicating that this transcription factor

609   was not involved in the remodeling we observed. In another study, myocardial deletion

610   of pyruvate dehydrogenase kinase 4 led to decreases in fatty acid oxidation and

611   increases in oxidation of pyruvate by mitochondria (48). Our results are not inconsistent

612   with those findings, but unlike our study the extent of cardiomyocyte proliferation in that

613   model did not produce an increase in HW/BW. Finally, we found no evidence of Hippo-

614   YAP/TAZ activation in the RISP KO hearts.

615   After myocardial ischemia in RISP KO hearts, projections of live cardiomyocytes

616   can be seen invading the infarcted region at day 60. By contrast, control hearts show

617   well-defined infarct borders without evidence of live cardiomyocytes within the injured

618   area. These findings therefore reveal the potential for repair of injured hearts in the

619   future. However, the progressive loss of RISP also causes a decline in cardiac function,

620   which becomes severe by 75 days and eventually leads to lethal cardiac failure. Future

621   studies are required to determine whether a restoration of *Uqcrfs1* in the injured heart

622   could restore RISP levels and mitochondrial function, reversing the contractile deficits

623   and allowing the newly formed cardiomyocytes in the infarct region to contribute to a

624   renewal of contractile function.

625   Malonate, a competitive inhibitor of complex II, was reported to extend the

626   proliferative window in neonatal cardiomyocytes and stimulate cardiomyocyte cell

627   division in adult mouse hearts after the induction of myocardial infarction (49).

628   Interesting similarities between that study and ours exist, although important differences

629   are also evident. Both studies induced a partial inhibition of mitochondrial function, Bae

630   et al. administered an inhibitor of complex II and ours involved genetic disruption of

631   complex III. Both studies observed metabolomic changes consistent with a shift toward

632 glycolysis, as expected based on the inhibitory effects on mitochondrial function. Unlike

633 Bae et al. we found an increase in glucose utilization and lactate accumulation, but

634 perhaps that reflects a more severe ETC inhibition with RISP deletion. Both studies

635 observed that newly formed cardiomyocytes are capable of repopulating myocardial

636 areas damaged by ischemia. However, one notable difference is that malonate only

637 increased adult cardiomyocyte proliferation in the context of infarction, whereas RISP

638 deletion caused a profound proliferative response throughout the heart, both in

639 ischemia-injured and in non-injured conditions. Given that malonate should affect

640 myocyte mitochondria similarly throughout the heart, the mechanism underlying the

641 localized proliferative response is not clear. Another difference relates to the

642 interpretation regarding the role of ROS and oxidative DNA damage. RISP deletion

643 attenuated oxidative stress in the hearts, and malonate would also be expected to

644 decrease ROS generation by the ETC. We used menadione to restore oxidant stress in

645 the hearts, which it did without blunting the hyperplastic remodeling, leading us to

646 conclude that decreases in oxidant stress were not responsible for the cardiomyocyte

647 proliferation caused by RISP KO. That observation, combined with the metabolomic

648 effects that favored developmental pathways driven by DNA methylation in the RISP KO

649 hearts, led us to conclude that the changes in metabolites caused by mitochondrial

650 inhibition were responsible for driving the remodeling. That conclusion is consistent

651 with the one reached by Bae et al..

652

653 **Methods**

654 Detailed methods can be found in the Supplementary materials.

655 *Animal studies*: Mice were housed under specific pathogen-free conditions in ventilated

656 cage racks in the Northwestern University animal facility under 12 hr light/dark cycling,

657 and were fed with standard lab chow, *ad libitum*, except where otherwise specified.

658 Myh6-Cre was activated using tamoxifen (0.5 mg, i.p. for 5 sequential days), after which

659 hearts were studied at 30, 60 and 75 days.

660 *Statistics*: Detailed statistical methodology can be found in the Supplementary

661 materials. The following statistical tests were employed and denoted in the Figure

662 Legends: an unpaired, 2-tailed T-test (U-2t-T-test); a Two-way ANOVA with a Sidak's

663 multiple comparison test (2W-ANOVA-Sidak's); a 2-tailed, Welch's Two-sample T-test

664 (2t-W-ts-T-test); an EdgeR-analysis (50); a Kolmogorov-Smirnov test; a generalized

665 linear model and ANOVA-like test; and a beta-binomial regression model with an

666 arcsine link function fitted using the generalized least square method and Wald-test. To

667 control for experimental differences in the responses, experimental studies and control

668 studies were always carried out on the same day. Statistical significance was set at

669 $p < 0.05$.

670 *Study approval*: All animal work was performed according to protocols approved by the

671 Northwestern University Institutional Animal Care and Use Committee.

672 *Sex as a biological variable*: All mouse studies included an equal number of male and

673 female animals, and similar findings are reported for both sexes.

674   *Data availability*: Gene expression data have been deposited in the NCBI GEO

675   database (accession GSE264439). A file with Supporting Data is available on the

676   *Journal* website, along with a file containing uncut gel images.

677

678   **Author Contributions**

679   GBW: DRS, CE, AQD, AD, WM

680   KAS: CE, AQD, AD

681   PTM: DRS, CE, AQD, AD

682   VJD: CE, AQD, AD

683   KAH: CE,AQD, AD, PR

684   BDS: DRS, AQD, AD, PR, WM

685   CBP: CE, AQD, AD, PR

686   JB: CE, AQD, PR

687   LN: AQD, AD

688   SJS: DRS, CE, AQD, AD, WM

689   GO: CE, AQD, AD

690   JAW: DRS, CE, AQD, AD, PR

691   WAM: AD

692   AVM: DRS, AQD, AD

693   GRSB: AQD, AD, PR

694   HA-V: AQD, AD, PR

695   NSC: DRS, WM

696   DD: CE, AQD, AD

697   EB: AD

698   SZ: CE, AQD, AD

699   YT: CE, PR

700   AM: CE, PR

701   HA: AD, PR

702   EBT: DRS, CE, AQD, AD, WM

703   PTS: DRS, CE, AQD, AD, WM

704

705   DRS: designing research studies, CE: conducting experiments, AQD: acquiring data,

706   AD: analyzing data, PR: providing reagents, and WM: writing the manuscript

707

708   **Acknowledgements**

References

737

738 1. Chandel NS, Maltepe E, Goldwasser E, Mathieu CE, Simon MC, and

739   Schumacker PT. Mitochondrial reactive oxygen species trigger hypoxia-induced

740   transcription. *Proc Natl Acad Sci USA.* 1998;95:11715-20.

741 2. Chen WW, Freinkman E, Wang T, Birsoy K, and Sabatini DM. Absolute

742   Quantification of Matrix Metabolites Reveals the Dynamics of Mitochondrial

743   Metabolism. *Cell.* 2016;166(5):1324-37 e11.

744 3. Raffaello A, Mammucari C, Gherardi G, and Rizzuto R. Calcium at the Center of

745   Cell Signaling: Interplay between Endoplasmic Reticulum, Mitochondria, and

746   Lysosomes. *Trends Biochem Sci.* 2016;41(12):1035-49.

747 4. Berendzen KM, Durieux J, Shao LW, Tian Y, Kim HE, Wolff S, et al.

748   Neuroendocrine Coordination of Mitochondrial Stress Signaling and Proteostasis.

749   *Cell.* 2016;166(6):1553-63 e10.

750 5. Yun J, and Finkel T. Mitohormesis. *Cell Metab.* 2014;19(5):757-66.

751 6. DeBerardinis RJ, and Chandel NS. Fundamentals of cancer metabolism. *Sci*

752   *Adv.* 2016;2(5):e1600200.

753 7. Chung S, Arrell DK, Faustino RS, Terzic A, and Dzeja PP. Glycolytic network

754   restructuring integral to the energetics of embryonic stem cell cardiac

755   differentiation. *J Mol Cell Cardiol.* 2010;48(4):725-34.

756 8. Lopaschuk GD, and Jaswal JS. Energy metabolic phenotype of the

757   cardiomyocyte during development, differentiation, and postnatal maturation. *J*

758   *Cardiovasc Pharmacol.* 2010;56(2):130-40.

759   9.   Chung S, Dzeja PP, Faustino RS, Perez-Terzic C, Behfar A, and Terzic A.

760   Mitochondrial oxidative metabolism is required for the cardiac differentiation of

761   stem cells. *Nat Clin Pract Cardiovasc Med.* 2007;4 Suppl 1:S60-7.

762   10.   Bhatti S, Zimmer G, and Bereiter-Hahn J. Enzyme release from chick myocytes

763   during hypoxia and reoxygenation: dependence on pH. *J Molec Cell Cardiol.*

764   1989;21(10):995-1008.

765   11.   St John JC, Ramalho-Santos J, Gray HL, Petrosko P, Rawe VY, Navara CS, et

766   al. The expression of mitochondrial DNA transcription factors during early

767   cardiomyocyte in vitro differentiation from human embryonic stem cells. *Cloning*

768   *Stem Cells.* 2005;7(3):141-53.

769   12.   Weinberg SE, Singer BD, Steinert EM, Martinez CA, Mehta MM, Martinez-Reyes

770   I, et al. Mitochondrial complex III is essential for suppressive function of

771   regulatory T cells. *Nature.* 2019;565(7740):495-9.

772   13.   Anso E, Weinberg SE, Diebold LP, Thompson BJ, Malinge S, Schumacker PT, et

773   al. The mitochondrial respiratory chain is essential for haematopoietic stem cell

774   function. *Nat Cell Biol.* 2017;19(6):614-25.

775   14.   Waypa GB, Marks JD, Guzy RD, Mungai PT, Schriewer JM, Dokic D, et al.

776   Superoxide generated at mitochondrial complex III triggers acute responses to

777   hypoxia in the pulmonary circulation. *Am J Respir Crit Care Med.*

778   2013;187(4):424-32.

779   15.   Sohal DS, Nghiem M, Crackower MA, Witt SA, Kimball TR, Tymitz KM, et al.

780   Temporally regulated and tissue-specific gene manipulations in the adult and

781   embryonic heart using a tamoxifen-inducible Cre protein. *Circ Res.*

782   2001;89(1):20-5.

783 16.   Muzumdar MD, Tasic B, Miyamichi K, Li L, and Luo L. A global double-

784   fluorescent Cre reporter mouse. *Genesis.* 2007;45(9):593-605.

785 17.   Chinopoulos C. Mitochondrial consumption of cytosolic ATP: not so fast. *FEBS*

786   *Lett.* 2011;585(9):1255-9.

787 18.   Hardie DG, Ross FA, and Hawley SA. AMPK: a nutrient and energy sensor that

788   maintains energy homeostasis. *Nat Rev Mol Cell Biol.* 2012;13(4):251-62.

789 19.   Merino D, Gil A, Gomez J, Ruiz L, Llano M, Garcia R, et al. Experimental

790   modelling of cardiac pressure overload hypertrophy: Modified technique for

791   precise, reproducible, safe and easy aortic arch banding-debanding in mice. *Sci*

792   *Rep.* 2018;8(1):3167.

793 20.   Puente BN, Kimura W, Muralidhar SA, Moon J, Amatruda JF, Phelps KL, et al.

794   The oxygen-rich postnatal environment induces cardiomyocyte cell-cycle arrest

795   through DNA damage response. *Cell.* 2014;157(3):565-79.

796 21.   Guzy RD, Hoyos B, Robin E, Chen H, Liu L, Mansfield KD, et al. Mitochondrial

797   complex III is required for hypoxia-induced ROS production and cellular oxygen

798   sensing. *Cell Metab.* 2005;1(6):401-8.

799 22.   Hanson GT, Aggeler R, Oglesbee D, Cannon M, Capaldi RA, Tsien RY, et al.

800   Investigating mitochondrial redox potential with redox-sensitive green fluorescent

801   protein indicators. *J Biol Chem.* 2004;279(13):13044-53.

802   23.   Bhuyan DK, Huang X, Kuriakose G, Garner WH, and Bhuyan KC. Menadione-

803   induced oxidative stress accelerates onset of Emory mouse cataract in vivo. *Curr*

804   *Eye Res.* 1997;16(6):519-26.

805   24.   Beck R, Verrax J, Dejeans N, Taper H, and Calderon PB. Menadione reduction

806   by pharmacological doses of ascorbate induces an oxidative stress that kills

807   breast cancer cells. *Int J Toxicol.* 2009;28(1):33-42.

808   25.   Argov Z, Bank WJ, Maris J, Eleff S, Kennaway NG, Olson RE, et al. Treatment of

809   mitochondrial myopathy due to complex III deficiency with vitamins K3 and C: A

810   31P-NMR follow-up study. *Ann Neurol.* 1986;19(6):598-602.

811   26.   Eleff S, Kennaway NG, Buist NR, Darley-Usmar VM, Capaldi RA, Bank WJ, et al.

812   31P NMR study of improvement in oxidative phosphorylation by vitamins K3 and

813   C in a patient with a defect in electron transport at complex III in skeletal muscle.

814   *Proc Natl Acad Sci U S A.* 1984;81(11):3529-33.

815   27.   Mahmoud AI, Kocabas F, Muralidhar SA, Kimura W, Koura AS, Thet S, et al.

816   Meis1 regulates postnatal cardiomyocyte cell cycle arrest. *Nature.*

817   2013;497(7448):249-53.

818   28.   Sabatini DM. Twenty-five years of mTOR: Uncovering the link from nutrients to

819   growth. *Proc Natl Acad Sci U S A.* 2017;114(45):11818-25.

820   29.   Saxton RA, and Sabatini DM. mTOR Signaling in Growth, Metabolism, and

821   Disease. *Cell.* 2017;169(2):361-71.

822   30.   Porta C, Paglino C, and Mosca A. Targeting PI3K/Akt/mTOR Signaling in

823   Cancer. *Front Oncol.* 2014;4:64.

824   31.   Moya IM, and Halder G. Hippo-YAP/TAZ signalling in organ regeneration and

825   regenerative medicine. *Nat Rev Mol Cell Biol.* 2019;20(4):211-26.

826   32.   Minois N, Carmona-Gutierrez D, and Madeo F. Polyamines in aging and disease.

827   *Aging (Albany NY).* 2011;3(8):716-32.

828   33.   Loenarz C, and Schofield CJ. Physiological and biochemical aspects of

829   hydroxylations and demethylations catalyzed by human 2-oxoglutarate

830   oxygenases. *Trends Biochem Sci.* 2011;36(1):7-18.

831   34.   Intlekofer AM, Dematteo RG, Venneti S, Finley LW, Lu C, Judkins AR, et al.

832   Hypoxia Induces Production of L-2-Hydroxyglutarate. *Cell Metab.*

833   2015;22(2):304-11.

834   35.   Intlekofer AM, Wang B, Liu H, Shah H, Carmona-Fontaine C, Rustenburg AS, et

835   al. L-2-Hydroxyglutarate production arises from noncanonical enzyme function at

836   acidic pH. *Nat Chem Biol.* 2017;13(5):494-500.

837   36.   McGrath-Morrow SA, Ndeh R, Helmin KA, Chen SY, Anekalla KR, Abdala-

838   Valencia H, et al. DNA methylation regulates the neonatal CD4(+) T-cell

839   response to pneumonia in mice. *J Biol Chem.* 2018;293(30):11772-83.

840   37.   Walter JM, Helmin KA, Abdala-Valencia H, Wunderink RG, and Singer BD.

841   Multidimensional assessment of alveolar T cells in critically ill patients. *JCI*

842   *Insight.* 2018;3(17):e123287.

843   38.   Singer BD. A Practical Guide to the Measurement and Analysis of DNA

844   Methylation. *Am J Respir Cell Mol Biol.* 2019;61(4):417-28.

845   39.   Morales-Nebreda L, Helmin KA, Torres Acosta MA, Markov NS, Hu JY, Joudi

846   AM, et al. Aging imparts cell-autonomous dysfunction to regulatory T cells during

847   recovery from influenza pneumonia. *JCI Insight.* 2021;6(6).

848   40.   Helmin KA, Morales-Nebreda L, Torres Acosta MA, Anekalla KR, Chen SY,

849   Abdala-Valencia H, et al. Maintenance DNA methylation is essential for

850   regulatory T cell development and stability of suppressive function. *J Clin Invest.*

851   2020;130(12):6571-87.

852   41.   El-Hattab AW, and Scaglia F. Mitochondrial Cardiomyopathies. *Front Cardiovasc*

853   *Med.* 2016;3:25.

854   42.   Lim DS, Roberts R, and Marian AJ. Expression profiling of cardiac genes in

855   human hypertrophic cardiomyopathy: insight into the pathogenesis of

856   phenotypes. *Journal of the American College of Cardiology.* 2001;38(4):1175-80.

857   43.   Alimadadi A, Munroe PB, Joe B, and Cheng X. Meta-Analysis of Dilated

858   Cardiomyopathy Using Cardiac RNA-Seq Transcriptomic Datasets. *Genes*

859   *(Basel).* 2020;11(1).

860   44.   Pritchard KA, Jr., Jing X, Teng M, Wells C, Jia S, Afolayan AJ, et al. Role of

861   endoplasmic reticulum stress in impaired neonatal lung growth and

862   bronchopulmonary dysplasia. *PLoS One.* 2022;17(8):e0269564.

863   45.   Orozco JM, Krawczyk PA, Scaria SM, Cangelosi AL, Chan SH, Kunchok T, et al.

864   Dihydroxyacetone phosphate signals glucose availability to mTORC1. *Nat*

865   *Metab.* 2020;2(9):893-901.

866   46.   Makinoshima H, Takita M, Saruwatari K, Umemura S, Obata Y, Ishii G, et al.

867   Signaling through the Phosphatidylinositol 3-Kinase (PI3K)/Mammalian Target of

868   Rapamycin (mTOR) Axis Is Responsible for Aerobic Glycolysis mediated by

869   Glucose Transporter in Epidermal Growth Factor Receptor (EGFR)-mutated

870   Lung Adenocarcinoma. *J Biol Chem.* 2015;290(28):17495-504.

871 47. Nguyen NUN, Canseco DC, Xiao F, Nakada Y, Li S, Lam NT, et al. A calcineurin-

872   Hoxb13 axis regulates growth mode of mammalian cardiomyocytes. *Nature.*

873   2020;582(7811):271-6.

874 48. Cardoso AC, Lam NT, Savla JJ, Nakada Y, Pereira AHM, Elnwasany A, et al.

875   Mitochondrial Substrate Utilization Regulates Cardiomyocyte Cell Cycle

876   Progression. *Nat Metab.* 2020;2(2):167-78.

877 49. Bae J, Salamon RJ, Brandt EB, Paltzer WG, Zhang Z, Britt EC, et al. Malonate

878   Promotes Adult Cardiomyocyte Proliferation and Heart Regeneration. *Circulation.*

879   2021;143(20):1973-86.

880 50. Robinson MD, McCarthy DJ, and Smyth GK. edgeR: a Bioconductor package for

881   differential expression analysis of digital gene expression data. *Bioinformatics.*

882   2010;26(1):139-40.

883

884

885   **Figure Legends**

886   **Figure 1.** Cardiac RISP KO and energy supply in mice. (**A**) Adult mT/mG reporter mice

887   carrying the Myh6-Cre transgene were administered tamoxifen. After 14 days, liver and

888   heart were removed and analyzed for evidence of Cre-mediated conversion from red to

889   green fluorescent protein. Liver expressed only red fluorescence, whereas cardiac

890   myocytes expressed green, indicating Cre activity. Scale bars: 50µm. (**B**) RISP KO and

891   WT mice were administered tamoxifen and then evaluated at 30-, 60- and 75-days. (**C,**

892   **D**) Immunoblotting heart lysates for RISP protein revealed a progressive loss, with

893   virtually complete depletion by 60 days, n=4 mice per condition, mean±SEM, 2W-

894   ANOVA-Sidak's. (**E, F**) Representative FDG-PET assessment in RISP WT and KO

895   mouse hearts. (**G**) Quantitative analysis of FDG utilization. The percent injected dose

896   (%ID) of FDG for each tissue was calculated by dividing the total PET signal found in

897   the region of interest by the injected dose for each mouse, n=4-5 mice per condition,

898   mean±SEM, U-2t-T-test. (**H**) Adenine nucleotide levels in snap-frozen hearts from RISP

899   WT and KO mice at 60- and 75-days post-tamoxifen, n=4 mice per condition,

900   mean±SEM, 2W-ANOVA-Sidak's. (**I**) Adenine nucleotide energy charge in snap-frozen

901   hearts from RISP WT and KO mice at 60- and 75-days post-tamoxifen, n=4 mice per

902   condition, mean±SEM, 2W-ANOVA-Sidak's. (**J, K**) Assessment of AMPK activation in in

903   snap-frozen hearts from RISP WT and KO mice at 60- and 75-days post-tamoxifen.

904   Positive control was rapidly excised and cooled prior to freezing, rather than snap-

905   frozen in situ, n=4 mice per condition, mean±SEM, U-2t-T-test. **p<0.01, ***p<0.001.

906

907   **Figure 2**. Cardiac RISP KO and subsequent remodeling in adult mice. (**A**) Heart size

908   increased significantly at 75 days post-tamoxifen in RISP KO mice, compared to WT

909   controls. Scale bars: 5mm. (**B**) HW/BW increased at 60- and 75-days post-tamoxifen in

910   RISP KO mice, compared with WT controls, n=6-9 mice per condition, mean±SEM, 2W-

911   ANOVA-Sidak's. (**C**) LV weight increased at 60- and 75-days post-tamoxifen,

912   compared with WT, n=6-9 mice per condition, mean±SEM, 2W-ANOVA-Sidak's. (**D**)

913   Heart size was significantly increased in RISP KO mice compared with WT, while cell

914   morphology was indistinguishable between groups. Scale bars: 2mm or 50µm. (**E**)

915   Cardiac fibrosis (Masson's trichrome stain) was absent in RISP KO hearts at 75 days

916   post-tamoxifen, and indistinguishable from WT. Cell diameter was assessed in PAS-

917   stained heart sections. Scale bars: 50µm. (**F**) Representative heart sections stained for

918   DAPI, myosin light chain (LC), and Ki-67 in RISP WT and KO hearts 60 days post-

919   tamoxifen. Yellow and magenta arrows denote Ki-67-positive nuclei. In hearts from

920   RISP WT mice, most Ki-67 positive nuclei were co-located to regions between

921   cardiomyocytes and therefore not counted (magenta arrows). In RISP KO hearts, only

922   Ki-67-positive nuclei that colocalized with cardiomyocytes were counted (yellow arrows).

923   Scale bars: 50µm. (**G**) Ki-67-positive nuclei were more abundant in RISP KO hearts at

924   60 days post-tamoxifen, compared with WT, n=8-18 mice per condition, mean±SEM,

925   2W-ANOVA-Sidak's. (**H**) phospho-H3-positive nuclei were more abundant in RISP KO

926   hearts at 60 days post-tamoxifen, compared with WT, n=8-18 mice per condition,

927   mean±SEM, 2W-ANOVA-Sidak's. (**I**) EdU-positive nuclei in cardiac sections from RISP

928   WT and KO mice at 60 days post-tamoxifen. EdU was administered by subcutaneous

929   micro-osmotic pump, inserted at day 30, n=3-6 mice per condition, mean±SEM, U-2t-T-

930   test. *p<0.05, ***p<0.001, ****p<0.0001.

931

932   **Figure 3**. Cardiac RISP deletion caused cardiac hyperplasia. (**A**) Isolated, individual

933   cardiomyocytes from mT/mG-RISP WT or KO mice 60 days post-tamoxifen were

934   stained with DAPI. Cardiomyocytes from mT/mG-RISP WT mice maintained red

935   fluorescence (mT), while cardiomyocytes from mT/mG-RISP KO mice expressed green

936   fluorescence (mG). The length and width of Cre-activated cardiomyocytes expressing

937   mG were measured (ImageJ). Scale bars: 25µm. Cardiomyocyte length (**B**) and width

938   (**C**), RISP KO had no effect on the size of cardiomyocytes compared to WT.

939   Approximately 40-45 cardiomyocytes per mouse were measured and averaged, n=6-10

940   mice per condition, mean±SEM, U-2t-T-test. (**D**) RISP KO caused cardiac hyperplasia

941   compared to WT, as assessed by the number of cardiomyocytes in the hearts.

942   Cardiomyocytes were counted and extrapolated to determine the number in the whole

943   heart, n=6-10 mice per condition, mean±SEM, U-2t-T-test. (**E**) RISP KO increased the

944   percentage of mononucleated and decreased percentage of binucleated

945   cardiomyocytes compared to WT. DAPI stained cardiomyocytes were imaged and

946   designated as mononucleated, binucleated, or polynucleated. Nuclei count is reported

947   as percentage of the assessed cardiomyocytes, (40-45 per mouse), n=6-10 mice per

948   condition, mean±SEM, U-2t-T-test. (**F**) RISP KO increased the total number of nuclei

949   compared to WT. Graph represents total number of nuclei per mouse heart and the

950   distribution of those nuclei across mono-, bi- and poly-nucleated cardiomyocytes, (40-45

951   per mouse), n=6-10 mice per condition, mean±SEM, U-2t-T-test. (**G**) Diagram

952 illustrating why cardiac wall thickness did not increase markedly in RISP KO hearts

953 undergoing hyperplastic remodeling. Cardiomyocytes appear to divide and grow in an

954 end-to-end direction rather than side-to-side (no difference in cell lengths), resulting in a

955 greater circumference of the heart wall without a large increase in LV wall thickness, or

956 a significant increase in the widths of the cells, or an increase in the number cells

957 across the LV free wall. ****$p<0.0001$.

958

959 **Figure 4**. Cardiac function studies. (**A**) LV fractional shortening, assessed by

960 echocardiography, decreased at 60 and 75 days post-tamoxifen in RISP KO hearts,

961 compared with WT, n=14-31 mice per condition, mean±SEM, 2W-ANOVA-Sidak's. (**B**)

962 LV ejection fraction decreased at 60 and 75 days post-tamoxifen in RISP KO, compared

963 with WT, n=14-31 mice per condition, mean±SEM, 2W-ANOVA-Sidak's. (**C**) LV end-

964 diastolic diameter increased at 60 and 75 days post-tamoxifen in RISP KO, compared

965 with WT, n=11-20 mice per condition, mean±SEM, 2W-ANOVA-Sidak's. (**D**) LV end-

966 systolic diameter increased at 60 and 75 days post-tamoxifen in RISP KO, compared

967 with WT, n=11-20 mice per condition, mean±SEM, 2W-ANOVA-Sidak's. (**E**) Heart rate

968 in RISP WT and RISP KO mice undergoing echocardiography at 30, 60 and 75 days

969 post-tamoxifen, n=11-20 mice per condition, mean±SEM, 2W-ANOVA-Sidak's. (**F**)

970 Stroke volume in RISP WT and KO mice at 30, 60 and 75 days post-tamoxifen, n=11-20

971 mice per condition, mean±SEM, 2W-ANOVA-Sidak's. (**G**) Cardiac output (product of

972 heart rate and end-diastolic minus end-systolic diameter), was not different between

973 RISP WT and KO hearts, n=11-20 mice per condition, mean±SEM, 2W-ANOVA-

974 Sidak's. (**H**) Hematocrit in RISP WT and KO mice at 30, 60 and 75 days post-tamoxifen,

975   n=4-9 mice per condition, mean±SEM, 2W-ANOVA-Sidak's.   **p<0.01, ***p<0.001,

976   ****p<0.0001.

977

978   **Figure 5**. New cardiomyocytes in RISP KO infiltrate regions of ischemic damage after

979   myocardial infarction (MI). The left anterior descending coronary artery was

980   permanently ligated 45 days post-tamoxifen thus creating a MI in the LV. At 60 days the

981   hearts were harvested, fixed, and serial-sliced from apex to base. (**A, D**) Representative

982   H&E-stained heart slices illustrating the MI-induced scar regions in the LV of RISP WT

983   and KO mice, respectively. Scale bars: 500µm. (**B, E**) Insets of (A) and (D),

984   respectively. ImageJ was used to trace the boundary between necrotic tissue and non-

985   necrotic to appreciate the geometry of the necrotic tissue. Finger-like projections of

986   dividing cardiomyocytes into the damaged tissue were observed in RISP KO hearts (E)

987   compared to the RISP WT heart (B). (**C, F**) Representative ellipses generated by

988   ImageJ designating the best fit ellipse based on the boundaries traced in (B) and (E),

989   respectively. (**G**) Quantitative analysis of the smoothness of the boundaries designating

990   the scar tissue calculated by dividing the measured parameters of the ellipses

991   generated in (C, F) by the measured parameters traced in (B, E), respectively.

992   Boundaries traced in RISP KO hearts were significantly rougher with more finger-like

993   projections of dividing cardiomyocytes migrating into the injured region compared to WT

994   hearts. Injured regions were traced in 6-8 heart slices/mouse with n=4 mice per

995   condition, mean±SEM, U-2t-T-test. (**H**) HW/BW of mice in MI studies demonstrated that

996   MI did not affect hyperplastic remodeling induced by RISP KO, n=4 mice per conditions,

997   mean±SEM, U-2t-T-test. (**I**) Differences in LV ejection fraction between RISP WT and

998   RISP KO mice were unaffected by the MI, compared with WT, n=4-14 mice per

999   condition, mean±SEM, U-2t-T-test. (**J**) Differences in LV fractional shortening between

1000 RISP WT and KO mice were unaffected by the MI, n=4-14 mice per condition,

1001 mean±SEM, U-2t-T-test. **p<0.01, ****p<0.0001.

1002

1003 **Figure 6**. mTOR phosphorylation of protein targets is consistent with the observation of

1004 proliferating cardiomyocytes. (**A**) Representative immunoblots of phosphorylated

1005 ribosomal S6 and ribosomal S6 from snap frozen heart homogenates from RISP WT

1006 and KO mice at 60 days post-tamoxifen. (**B**) Band density analysis of phosphorylated

1007 ribosomal S6 and ribosomal S6 from RISP WT and KO mice at 60 days post-tamoxifen,

1008 n=12 mice per condition, mean±SEM, U-2t-T-test. (**C**) Representative immunoblots of

1009 phosphorylated S6 kinase and S6 kinase from RISP WT and KO mice at 60 days post-

1010 tamoxifen. (**D**) Band density analysis of phosphorylated S6 kinase and S6 kinase from

1011 RISP WT and KO mice at 60 days post-tamoxifen, n=8 mice per condition, mean±SEM,

1012 U-2t-T-test. (**E**) Representative immunoblots of phosphorylated (pAkt) and total Akt from

1013 RISP WT and KO mice at 60 days post-tamoxifen. (**F**) Band density analysis of pAkt

1014 and total Akt from RISP WT and KO mice at 60 days post-tamoxifen, n=4 mice per

1015 condition, mean±SEM, U-2t-T-test. *p<0.05, **p<0.01, ****p<0.0001.

1016

1017 **Figure 7**. Transcriptomic responses in RISP WT and KO hearts at 60 days post-

1018 tamoxifen. (**A**) Principal component analysis of RNA-seq data from RISP WT and KO

1019 hearts. (**B**) K-means 2 clustering of gene expression values for 1355 differentially

1020   expressed genes in RISP WT (n=4 mice, left columns) and KO (n=4 mice, right

1021   columns) (adjusted p<0.05, EdgeR-analysis) (red: increased expression relative to

1022   blue).

1023

1024   **Figure 8**. (**A**) Ca^{2+} measurements in paced cardiomyocytes revealed that the initial rise

1025   in Ca^{2+} was indistinguishable between RISP WT and KO mice. However, sequestration

1026   of Ca^{2+} was faster in the KO cardiomyocytes compared to WT. Further analysis of Ca^{2+}

1027   dynamics is presented in Supplementary figure S9A-H. (**B**) Immunoblotting for MyLK3

1028   protein revealed a decrease in RISP KO compared to WT hearts at 60 days post-

1029   tamoxifen (**C**) Band density analysis of immunoblots of MyLK3 and GAPDH in RISP WT

1030   and KO hearts at 60 post-tamoxifen, n=7 mice per condition, mean±SEM, U-2t-T-test.

1031   ***p<0.001.

1032

1033   **Figure 9.** Metabolomic responses in RISP WT and KO hearts at 60 days post-

1034   tamoxifen. (**A**) Analysis of glycolytic and TCA cycle biomolecules revealed significant

1035   increases in glycolytic intermediates (red) and decreased abundance of TCA cycle

1036   components (green) in RISP KO, compared to WT hearts (p<0.05. 2t-W-ts-T-test). (**B**)

1037   Analysis of biomolecules involved in membrane synthesis revealed increases in

1038   phosphatidylcholine and phosphatidylenthaolamine (red), along with decreases in

1039   substrates feeding into their synthesis (green) in RISP KO, compared to WT hearts

1040   (p<0.05, 2t-W-ts-T-test). (**C**) Analysis of polyamines revealed increases in putrescine,

1041   spermidine, MTA and N-acytylspermidine (red) in RISP KO, compared to WT hearts

1042   (p<0.05, 2t-W-ts-T-test). (**D**) Analysis of fatty acid oxidation intermediates revealed

1043   increases in acyl-carnitines (red) in RISP KO, compared to WT hearts (p<0.05, 2t-W-ts-

1044   T-test). (**E**) Scaled ratio of biochemical factors that promote DNA methylation in RISP

1045   WT (blue) and KO hearts (red), n=8 mice per condition, mean±SEM, U-2t-T-test.

1046   *p<0.05, **p<0.01, ****p<0.0001.

1047

1048   **Figure 10.** Epigenetic analysis of RISP WT and KO hearts. (**A**) Left: Cumulative

1049   distribution of DNA CpG methylation in RISP WT (blue) and KO (red) hearts. Right:

1050   Box-whisker plot showing significant increase in DNA CpG methylation (DMC) in RISP

1051   KO compared with WT hearts (p<0.0001, Kolmogorov-Smirnov test). (**B**) Venn diagram

1052   comparing differentially expressed genes (DEG) and differentially methylated DNA CpG

1053   sites located in regulatory regions of genes, reveals an overlap of 115 genes. (**C**) K-

1054   means clustering of RNA-seq identification of 115 DEG and DMC genes showing

1055   directional change (up- (red) vs. down- (blue) regulated) in RISP KO (n=4) versus WT

1056   hearts (n=4). (**D**) K-means clustering after filtering was applied to restrict the dataset to

1057   CpGs with 25% higher methylation in lower expression groups compared with higher

1058   expression groups; this identified 93 DEG and DMC genes in RISP KO (n=4) versus WT

1059   hearts. (**E**) DNA CpG methylation status of 93 DMC and DEG showing that down-

1060   regulated genes are more highly methylated (green) in regulatory regions, while up-

1061   regulated genes are less highly methylated (violet), in RISP KO compared with WT. For

1062   panels C-E, DEG were determined using a generalized linear model and ANOVA-like

1063   testing with FDR q-value < 0.05, and DMC were determined using a beta-binomial

1064   regression model with an arcsine link function fitted using the generalized least square

1065   method and Wald-test FDR q-value < 0.05.

1066

1067   **Table 1. Mitochondrial unfolded protein response**

1068   Upregulated

Gene Identifier	Gene Name	Adjusted p value	Log fold change
Atf3	activating transcription factor 3	9.78E-37	4.07
Atf4	activating transcription factor 4	5.22E-10	1.60
Atf5	activating transcription factor 5	1.17E-3	1.04
Fgf21	fibroblast growth factor 21	6.89E-8	6.87
Gdf15	growth differentiation factor 15	1.09E-16	5.08
Mthfd2	methylenetetrahydrofolate dehydrogenase (NAD+ dependent)	6.38E-23	3.86

1069

1070

1071 **Table 2. Gene ontology biological processes**
1072 **Upregulated**

Biological Process	Adjusted p value	Log.p
system development	1.97E-06	9.485322111
cardiovascular system development	1.97E-06	9.231834183
circulatory system development	1.97E-06	9.231834183
anatomical structure development	1.97E-06	9.09116447
multicellular organismal development	4.88E-06	8.486651865
blood vessel development	1.05E-05	8.006687241
vasculature development	1.09E-05	7.905197076
cell proliferation	1.35E-05	7.805893781
angiogenesis	3.27E-05	7.324129129
developmental process	3.66E-05	7.225317377
tissue development	3.66E-05	7.205878086
extracellular matrix organization	0.000113644	6.607788603
blood vessel morphogenesis	0.000158945	6.413026952
organ development	0.00025163	6.180633767
organ regeneration	0.000438991	5.875020007
muscle structure development	0.00109098	5.444199641
striated muscle tissue development	0.00210116	5.095058442
skeletal muscle tissue development	0.00226321	5.050069657
cell differentiation	0.0023638	5.017679912
regulation of cell proliferation	0.002453	4.971445013
skeletal muscle organ development	0.00279358	4.872221596
muscle tissue development	0.0035457	4.741654899
anatomical structure morphogenesis	0.00483505	4.565459837
muscle organ development	0.00523413	4.507203305

regeneration	0.00523413	4.502505031
positive regulation of cell proliferation	0.00933079	4.221424073
regulation of developmental process	0.0140077	4.016288937
positive regulation of cell migration	0.0156637	3.953789776
regulation of multicellular organismal development	0.0156637	3.945042404
glucose metabolic process	0.0168843	3.905043488
cellular component organization	0.018803	3.842815318
positive regulation of cell motility	0.0199197	3.82610603
response to unfolded protein	0.0319113	3.574738114
cellular component organization or biogenesis	0.038271	3.474873527
negative regulation of cell death	0.0408694	3.435544626

1073

1074 **Table 3. Gene ontology biological processes**
1075 **Downregulated**

regulation of cardiac muscle contraction	0.0150692	5.545808
regulation of muscle system process	0.0150692	5.481011
regulation of striated muscle contraction	0.0183851	5.055738
muscle adaptation	0.0183851	5.022691
cardiac muscle contraction	0.0183851	4.878939
striated muscle contraction	0.0190922	4.757812
circulatory system process	0.0190922	4.676839
regulation of heart contraction	0.0295475	4.461484

1076

1077

1078 **Table 4.   Altered expression in growth factor signaling**

1079 **Upregulated**

1080

Gene Name	Gene Identifier	Adjusted p value	Log fold change
heparin-binding EGF-like growth factor	*Hbegr*	5.52E-13	2.11
insulin-like growth factor binding protein 7	*Igfbp7*	2.26E-8	1.42
fibroblast growth factor 21	*Fgf*	6.89E-8	6.87
insulin-like growth factor 1	*Igf1*	2.31E-6	1.73
connective tissue growth factor	*Ctgf*	1.10E-5	1.44
insulin-like growth factor 2 mRNA binding protein 2	*Igf2bp2*	2.34E-3	1.30

1081 ## Downregulated

insulin-like growth factor binding protein, acid labile subunit	*Igfals*	4.71E-4	-1.86
insulin-like growth factor binding protein 3	*Igfbp3*	3.23E-3	-1.32
epidermal growth factor	*Egf*	3.71E-3	-1.21
fibroblast growth factor 12	*Fgf12*	4.00E-3	-1.85

1082
1083

Table 5.   GO pathway analysis: Upregulated process in DMC and DEG overlap gene set

Biological Process	# in overlap	p-value	FDR q-value
GO_ACTIN_FILAMENT_BASED_PROCESS	7	9.67E-08	4.29E-04
GO_MUSCLE_STRUCTURE_DEVELOPMENT	6	1.67E-06	2.58E-03
GO_MUSCLE_CELL_DIFFERENTIATION	5	1.74E-06	2.58E-03
GO_CARDIAC_MUSCLE_TISSUE_DEVELOPMENT	4	6.25E-06	6.93E-03
GO_MYOFIBRIL_ASSEMBLY	3	9.52E-06	8.44E-03
GO_PROTEIN_PHOSPHORYLATION	7	1.31E-05	9.12E-03
GO_STRIATED_MUSCLE_CELL_DIFFERENTIATION	4	1.44E-05	9.12E-03
GO_BIOLOGICAL_ADHESION	7	2.32E-05	1.29E-02
GO_ACTOMYOSIN_STRUCTURE_ORGANIZATION	3	3.96E-05	1.71E-02
GO_INTRACELLULAR_SIGNAL_TRANSDUCTION	8	4.40E-05	1.71E-02
GO_HEART_DEVELOPMENT	5	4.55E-05	1.71E-02
GO_REGULATION_OF_ANATOMICAL_STRUCTURE_SIZE	5	4.83E-05	1.71E-02
GO_CIRCULATORY_SYSTEM_DEVELOPMENT	6	5.02E-05	1.71E-02
GO_PHOSPHORYLATION	7	6.96E-05	2.03E-02
GO_CYTOSKELETON_ORGANIZATION	6	7.05E-05	2.03E-02
GO_GLYCOPROTEIN_CATABOLIC_PROCESS	2	7.32E-05	2.03E-02
GO_MUSCLE_TISSUE_DEVELOPMENT	4	8.75E-05	2.28E-02
GO_MUSCLE_SYSTEM_PROCESS	4	9.64E-05	2.38E-02
GO_CELL_MATRIX_ADHESION	3	1.45E-04	3.37E-02
GO_CELL_DEVELOPMENT	7	1.76E-04	3.79E-02
GO_MUSCLE_CELL_DEVELOPMENT	3	1.79E-04	3.79E-02
GO_REGULATION_OF_CELLULAR_COMPONENT_SIZE	4	1.91E-04	3.85E-02
GO_SMALL_GTPASE_MEDIATED_SIGNAL_TRANSDUCTION	4	2.25E-04	4.34E-02

55

GO_SARCOMERE_ORGANIZATION	2	2.43E-04	4.49E-02
GO_TISSUE_DEVELOPMENT	7	2.58E-04	4.57E-02

1086

1087

Table 6.   GO pathway analysis: Downregulated process in DMC and DEG overlap gene set

1088
1089
1090

Biological Process	# in overlap	P-value	FDR q-value
GO_REGULATION_OF_TRANSCRIPTION_FROM_RNA_ POLYMERASE_II_PROMOTER	12	4.80E-06	6.94E-03
GO_SYSTEM_PROCESS	12	4.82E-06	6.94E-03
GO_CELLULAR_RESPONSE_TO_NITROGEN_COMPOUND	7	6.04E-06	6.94E-03
GO_REGULATION_OF_HEART_RATE	4	6.26E-06	6.94E-03
GO_MOVEMENT_OF_CELL_OR_SUBCELLULAR_ COMPONENT	10	8.77E-06	7.78E-03
GO_RESPONSE_TO_CAMP	4	1.33E-05	9.26E-03
GO_GLAND_DEVELOPMENT	6	1.74E-05	9.26E-03
GO_MEMBRANE_DEPOLARIZATION_DURING_ACTION_ POTENTIAL	3	2.17E-05	9.26E-03
GO_CELL_DEVELOPMENT	10	2.30E-05	9.26E-03
GO_TAXIS	6	4.28E-05	1.46E-02
GO_CELLULAR_RESPONSE_TO_INSULIN_STIMULUS	4	5.03E-05	1.52E-02
GO_ION_TRANSPORT	9	5.39E-05	1.52E-02
GO_POSITIVE_REGULATION_OF_RESPONSE_TO_STIMULUS	11	5.70E-05	1.52E-02

GO_NEGATIVE_REGULATION_OF_MULTICELLULAR_ ORGANISMAL_PROCESS	8	5.83E-05	1.52E-02
GO_CELLULAR_RESPONSE_TO_ENDOGENOUS_STIMULUS	8	6.94E-05	1.62E-02
GO_REGULATION_OF_MEMBRANE_POTENTIAL	5	1.11E-04	2.14E-02
GO_CELLULAR_RESPONSE_TO_OXYGEN_CONTAINING_ COMPOUND	7	1.11E-04	2.14E-02
GO_REGULATION_OF_CYTOKINE_PRODUCTION	6	1.24E-04	2.14E-02
GO_TRANSMEMBRANE_TRANSPORT	8	1.25E-04	2.14E-02
GO_ION_TRANSMEMBRANE_TRANSPORT	7	1.32E-04	2.14E-02
GO_LOCOMOTION	8	1.38E-04	2.14E-02
GO_INORGANIC_ION_TRANSMEMBRANE_TRANSPORT	6	1.50E-04	2.14E-02
GO_CIRCULATORY_SYSTEM_PROCESS	5	1.50E-04	2.14E-02
GO_POSITIVE_REGULATION_OF_MOLECULAR_FUNCTION	10	1.53E-04	2.14E-02
GO_RESPONSE_TO_ENDOGENOUS_STIMULUS	9	1.54E-04	2.14E-02
GO_REGULATION_OF_TRANSPORT	10	1.62E-04	2.17E-02
GO_POSITIVE_REGULATION_OF_CELLULAR_COMPONENT_ORGANIZATION	8	1.74E-04	2.20E-02
GO_RESPONSE_TO_INSULIN	4	1.86E-04	2.23E-02
GO_REGULATION_OF_CELL_DIFFERENTIATION	9	1.91E-04	2.23E-02
GO_CELLULAR_RESPONSE_TO_ORGANIC_SUBSTANCE	10	1.97E-04	2.23E-02

GO_CARDIAC_CONDUCTION	3	2.01E-04	2.23E-02
GO_HEART_PROCESS	3	2.24E-04	2.42E-02
GO_REGULATION_OF_HEART_CONTRACTION	4	2.48E-04	2.56E-02
GO_REGULATION_OF_INTRACELLULAR_SIGNAL_TRANSDUCTION	9	4.11E-04	3.88E-02
GO_REGULATION_OF_ANATOMICAL_STRUCTURE_MORPHOGENESIS	7	4.91E-04	4.44E-02
GO_BIOLOGICAL_ADHESION	7	5.23E-04	4.50E-02

1091
1092

1093

Table 7. Genes passing methylation filter

2410066E13Rik	Dixdc1	Mylk3	Bcl11b	Scn10a	Sh2d4a	Bmp2k	Kcng4
Ano10	Fign	Trabd2b	Hmgcs2	4930529M08Rik	Rab30	Nrep	Syndig1
Cngb3	Nudt4	D3Ertd751e	Cacna2d1	Slc26a3	Ankrd1	Pcdh17	Nars
1110034G24Rik	Mpped2	Rbfox1	Neo1	Opcml	Diap1	Adamts9	Tshz2
Cntn5	Tfpi	Antxr2	Tbc1d4	Psd3	Dnaja4	Fam129a	Actn2
Angpt1	Yipf7	Asb15	Abhd13	Cilp2	Fbxo40	Pxk	Xirp2
Egflam	Cacnb2	Zdhhc17	Slco5a1	Tmem108	Cald1	Hells	Postn
Gm26905	Aldh4a1	Zfp46	Tmtc1	Tmem163	Igfbp7	Myo1e	Thbs4
A730061H03Rik	Fbxw7	Lrrc3b	Pde4d	Shisa6	Lmod3	Map3k4	Slc26a7
Ttc7	Gata6	Fam65b	Zbtb20	Setbp1	Ttll11	Rasgrp3	
Pla2g5	Ak4	Aox1	Rps6ka5	Tmem56	Arhgap18	Sik1	
Cbx7	Cpeb3	Gm20619	Rreb1	2010111I01Rik	Rab37	Eif2s2	

1095

1096

1097

1098

1099 **Figures**
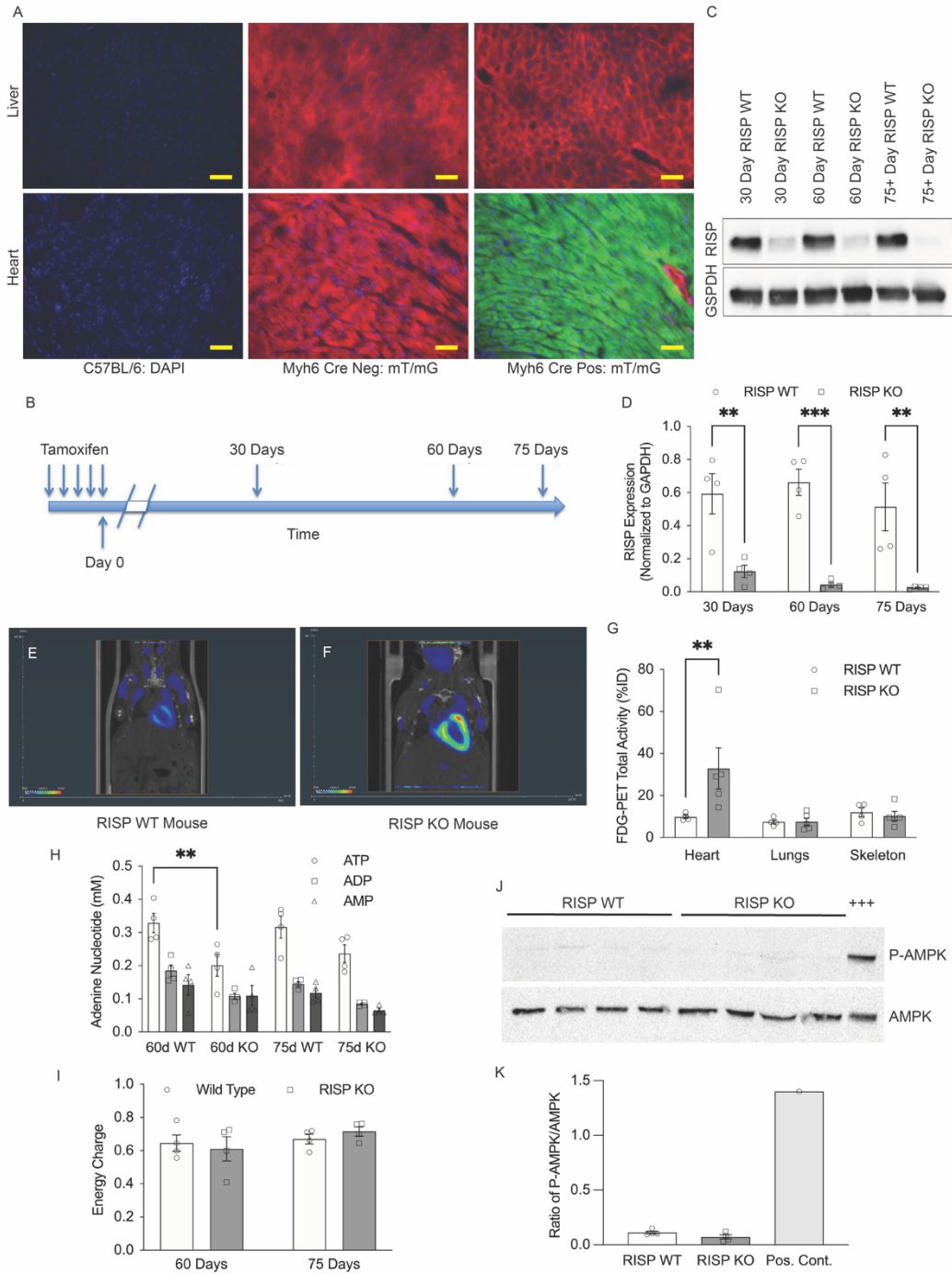
1100

1101

1102   **Figure 1.** Cardiac RISP KO and energy supply in mice. (**A**) Adult mT/mG reporter mice

1103   carrying the Myh6-Cre transgene were administered tamoxifen. After 14 days, liver and

1104   heart were removed and analyzed for evidence of Cre-mediated conversion from red to

1105   green fluorescent protein. Liver expressed only red fluorescence, whereas cardiac

1106   myocytes expressed green, indicating Cre activity. Scale bars: 50μm. (**B**) RISP KO and

1107   WT mice were administered tamoxifen and then evaluated at 30-, 60- and 75-days. (**C,**

1108   **D**) Immunoblotting heart lysates for RISP protein revealed a progressive loss, with

1109   virtually complete depletion by 60 days, n=4 mice per condition, mean±SEM, 2W-

1110   ANOVA-Sidak's. (**E, F**) Representative FDG-PET assessment in RISP WT and KO

1111   mouse hearts. (**G**) Quantitative analysis of FDG utilization. The percent injected dose

1112   (%ID) of FDG for each tissue was calculated by dividing the total PET signal found in

1113   the region of interest by the injected dose for each mouse, n=4-5 mice per condition,

1114   mean±SEM, U-2t-T-test. (**H**) Adenine nucleotide levels in snap-frozen hearts from RISP

1115   WT and KO mice at 60- and 75-days post-tamoxifen, n=4 mice per condition,

1116   mean±SEM, 2W-ANOVA-Sidak's. (**I**) Adenine nucleotide energy charge in snap-frozen

1117   hearts from RISP WT and KO mice at 60- and 75-days post-tamoxifen, n=4 mice per

1118   condition, mean±SEM, 2W-ANOVA-Sidak's. (**J, K**) Assessment of AMPK activation in in

1119   snap-frozen hearts from RISP WT and KO mice at 60- and 75-days post-tamoxifen.

1120   Positive control was rapidly excised and cooled prior to freezing, rather than snap-

1121   frozen in situ, n=4 mice per condition, mean±SEM, U-2t-T-test. **p<0.01, ***p<0.001.

1122

1123
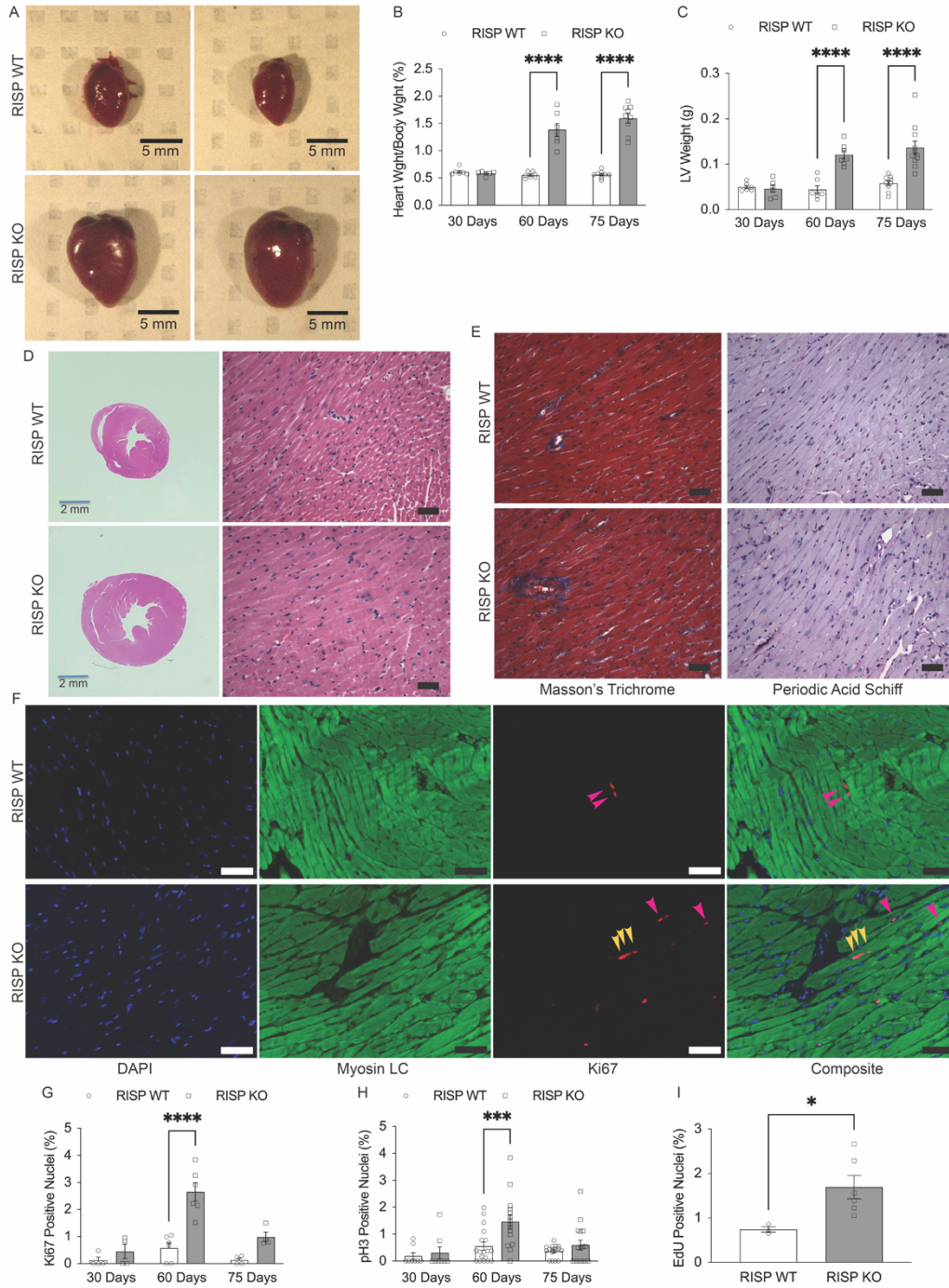
1124

1125 **Figure 2**. Cardiac RISP KO and subsequent remodeling in adult mice. (**A**) Heart size

1126 increased significantly at 75 days post-tamoxifen in RISP KO mice, compared to WT

1127 controls. Scale bars: 5mm. (**B**) HW/BW increased at 60- and 75-days post-tamoxifen in

1128 RISP KO mice, compared with WT controls, n=6-9 mice per condition, mean±SEM, 2W-

1129 ANOVA-Sidak's. (**C**) LV weight increased at 60- and 75-days post-tamoxifen,

1130 compared with WT, n=6-9 mice per condition, mean±SEM, 2W-ANOVA-Sidak's. (**D**)

1131 Heart size was significantly increased in RISP KO mice compared with WT, while cell

1132 morphology was indistinguishable between groups. Scale bars: 2mm or 50µm. (**E**)

1133 Cardiac fibrosis (Masson's trichrome stain) was absent in RISP KO hearts at 75 days

1134 post-tamoxifen, and indistinguishable from WT. Cell diameter was assessed in PAS-

1135 stained heart sections. Scale bars: 50µm. (**F**) Representative heart sections stained for

1136 DAPI, myosin light chain (LC), and Ki-67 in RISP WT and KO hearts 60 days post-

1137 tamoxifen. Yellow and magenta arrows denote Ki-67-positive nuclei. In hearts from

1138 RISP WT mice, most Ki-67 positive nuclei were co-located to regions between

1139 cardiomyocytes and therefore not counted (magenta arrows). In RISP KO hearts, only

1140 Ki-67-positive nuclei that colocalized with cardiomyocytes were counted (yellow arrows).

1141 Scale bars: 50µm. (**G**) Ki-67-positive nuclei were more abundant in RISP KO hearts at

1142 60 days post-tamoxifen, compared with WT, n=8-18 mice per condition, mean±SEM,

1143 2W-ANOVA-Sidak's. (**H**) phospho-H3-positive nuclei were more abundant in RISP KO

1144 hearts at 60 days post-tamoxifen, compared with WT, n=8-18 mice per condition,

1145 mean±SEM, 2W-ANOVA-Sidak's. (**I**) EdU-positive nuclei in cardiac sections from RISP

1146 WT and KO mice at 60 days post-tamoxifen. EdU was administered by subcutaneous

1147   micro-osmotic pump, inserted at day 30, n=3-6 mice per condition, mean±SEM, U-2t-T-

1148   test. $*p<0.05$, $***p<0.001$, $****p<0.0001$.

1149
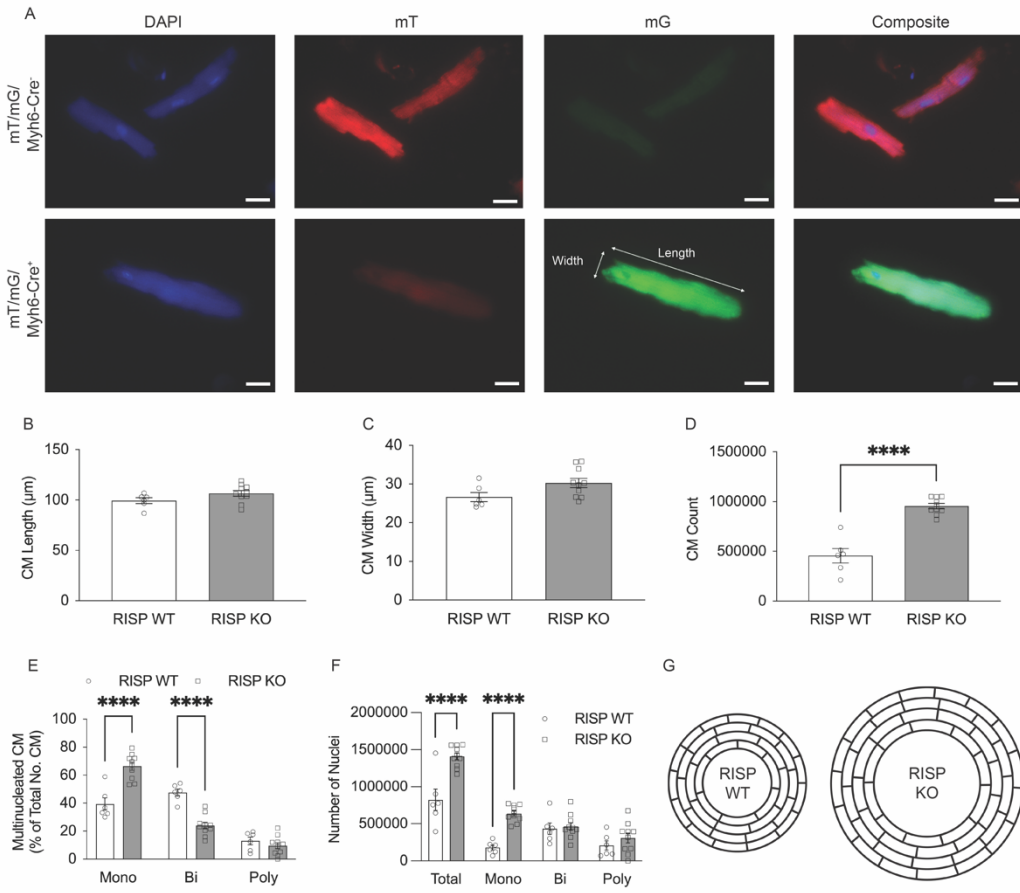
1150

1151   **Figure 3**. Cardiac RISP deletion caused cardiac hyperplasia. (**A**) Isolated, individual

1152   cardiomyocytes from mT/mG-RISP WT or KO mice 60 days post-tamoxifen were

1153   stained with DAPI. Cardiomyocytes from mT/mG-RISP WT mice maintained red

1154   fluorescence (mT), while cardiomyocytes from mT/mG-RISP KO mice expressed green

1155   fluorescence (mG). The length and width of Cre-activated cardiomyocytes expressing

1156   mG were measured (ImageJ). Scale bars: 25µm. Cardiomyocyte length (**B**) and width

1157   (**C**), RISP KO had no effect on the size of cardiomyocytes compared to WT.

1158   Approximately 40-45 cardiomyocytes per mouse were measured and averaged, n=6-10

1159   mice per condition, mean±SEM, U-2t-T-test. (**D**) RISP KO caused cardiac hyperplasia

1160   compared to WT, as assessed by the number of cardiomyocytes in the hearts.

1161   Cardiomyocytes were counted and extrapolated to determine the number in the whole

1162   heart, n=6-10 mice per condition, mean±SEM, U-2t-T-test. (**E**) RISP KO increased the

1163   percentage of mononucleated and decreased percentage of binucleated

1164   cardiomyocytes compared to WT. DAPI stained cardiomyocytes were imaged and

1165   designated as mononucleated, binucleated, or polynucleated. Nuclei count is reported

1166   as percentage of the assessed cardiomyocytes, (40-45 per mouse), n=6-10 mice per

1167   condition, mean±SEM, U-2t-T-test. (**F**) RISP KO increased the total number of nuclei

1168   compared to WT. Graph represents total number of nuclei per mouse heart and the

1169   distribution of those nuclei across mono-, bi- and poly-nucleated cardiomyocytes, (40-45

1170   per mouse), n=6-10 mice per condition, mean±SEM, U-2t-T-test. (**G**) Diagram

1171   illustrating why cardiac wall thickness did not increase markedly in RISP KO hearts

1172   undergoing hyperplastic remodeling. Cardiomyocytes appear to divide and grow in an

1173   end-to-end direction rather than side-to-side (no difference in cell lengths), resulting in a

1174   greater circumference of the heart wall without a large increase in LV wall thickness, or

1175   a significant increase in the widths of the cells, or an increase in the number cells

1176   across the LV free wall. ****$p < 0.0001$.

1177

1178
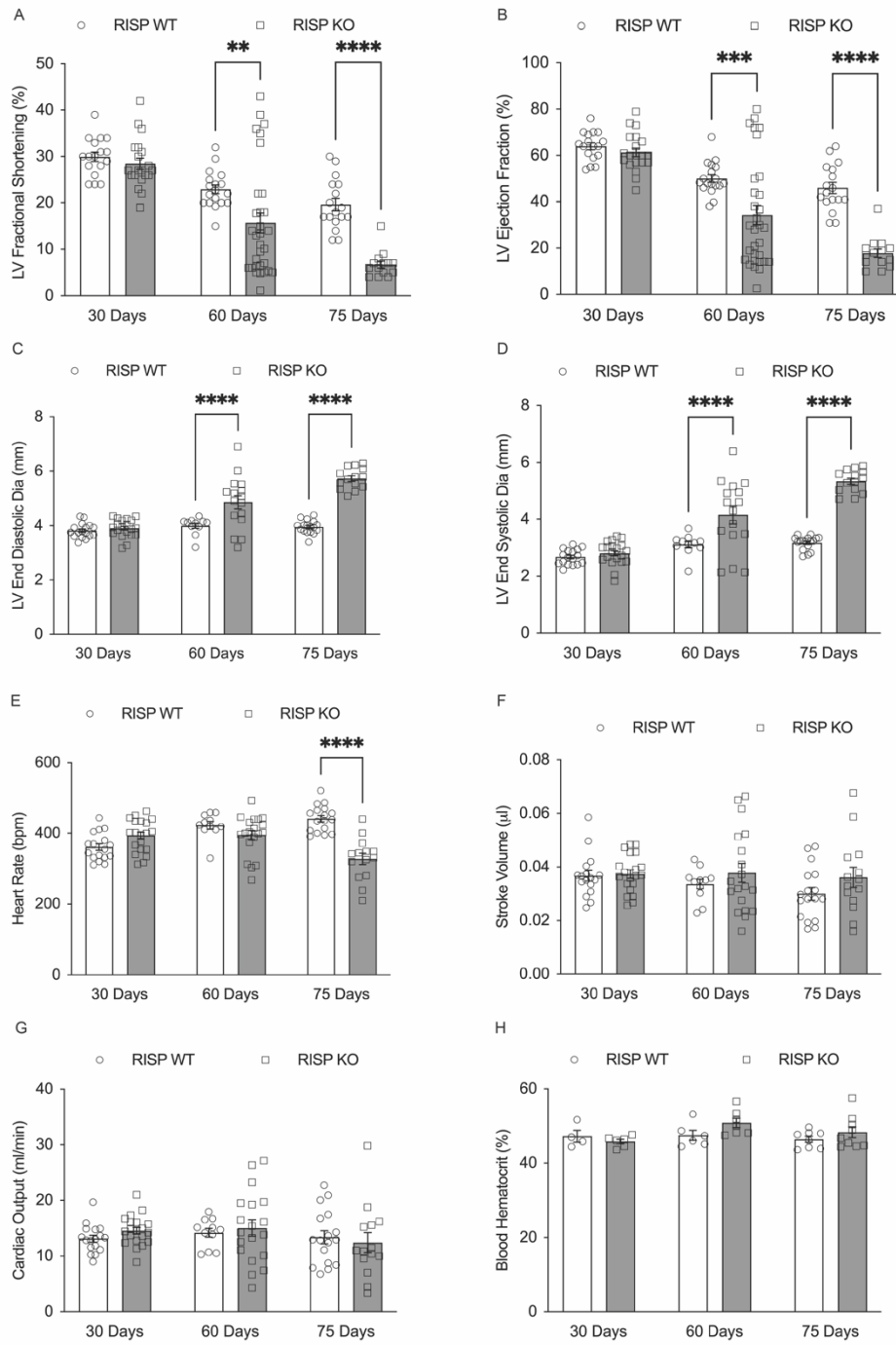
1179

1180

1181   **Figure 4**. Cardiac function studies. (**A**) LV fractional shortening, assessed by

1182   echocardiography, decreased at 60 and 75 days post-tamoxifen in RISP KO hearts,

1183   compared with WT, n=14-31 mice per condition, mean±SEM, 2W-ANOVA-Sidak's. (**B**)

1184   LV ejection fraction decreased at 60 and 75 days post-tamoxifen in RISP KO, compared

1185   with WT, n=14-31 mice per condition, mean±SEM, 2W-ANOVA-Sidak's. (**C**) LV end-

1186   diastolic diameter increased at 60 and 75 days post-tamoxifen in RISP KO, compared

1187   with WT, n=11-20 mice per condition, mean±SEM, 2W-ANOVA-Sidak's. (**D**) LV end-

1188   systolic diameter increased at 60 and 75 days post-tamoxifen in RISP KO, compared

1189   with WT, n=11-20 mice per condition, mean±SEM, 2W-ANOVA-Sidak's. (**E**) Heart rate

1190   in RISP WT and RISP KO mice undergoing echocardiography at 30, 60 and 75 days

1191   post-tamoxifen, n=11-20 mice per condition, mean±SEM, 2W-ANOVA-Sidak's. (**F**)

1192   Stroke volume in RISP WT and KO mice at 30, 60 and 75 days post-tamoxifen, n=11-20

1193   mice per condition, mean±SEM, 2W-ANOVA-Sidak's. (**G**) Cardiac output (product of

1194   heart rate and end-diastolic minus end-systolic diameter), was not different between

1195   RISP WT and KO hearts, n=11-20 mice per condition, mean±SEM, 2W-ANOVA-

1196   Sidak's. (**H**) Hematocrit in RISP WT and KO mice at 30, 60 and 75 days post-tamoxifen,

1197   n=4-9 mice per condition, mean±SEM, 2W-ANOVA-Sidak's.   **p<0.01, ***p<0.001,
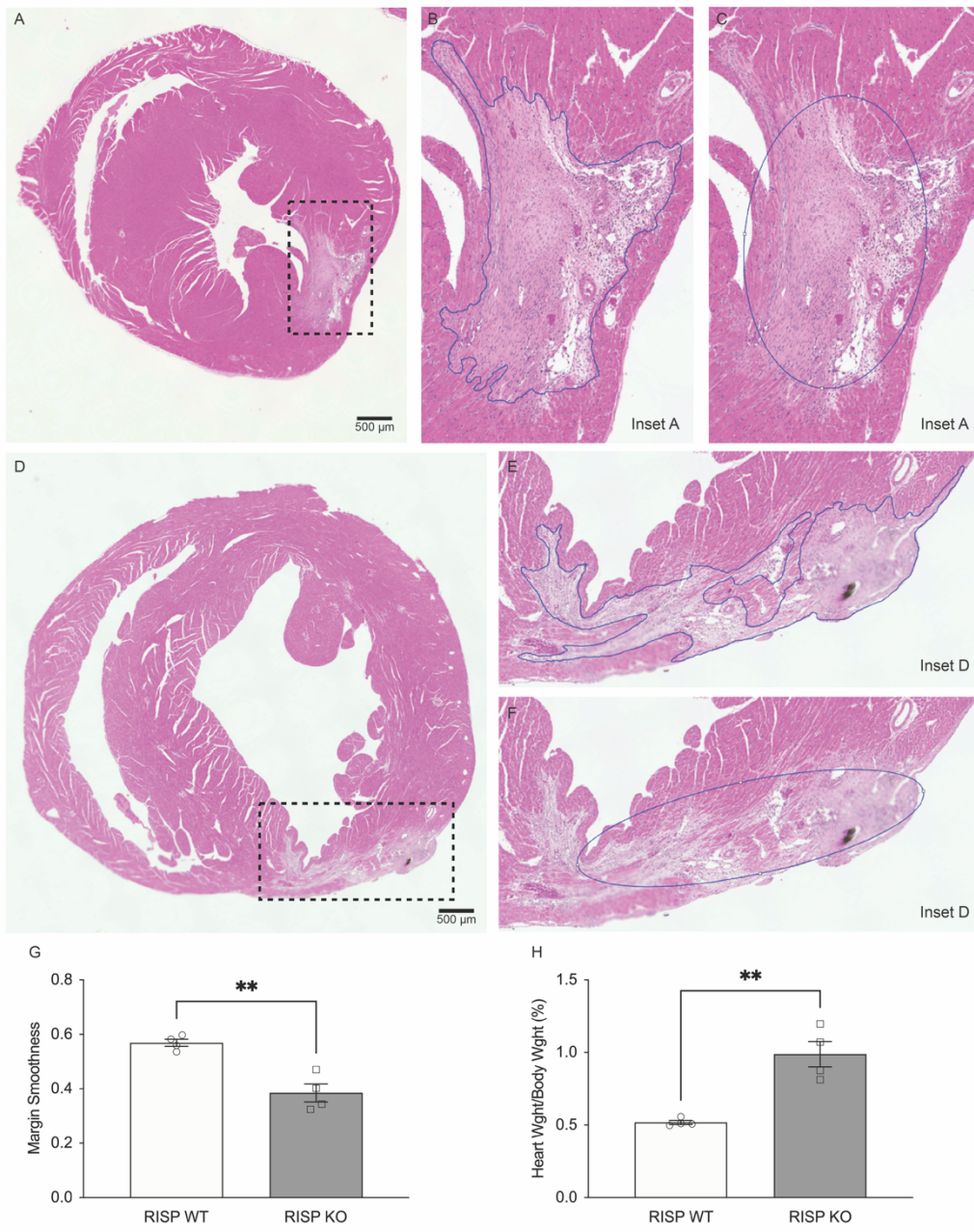
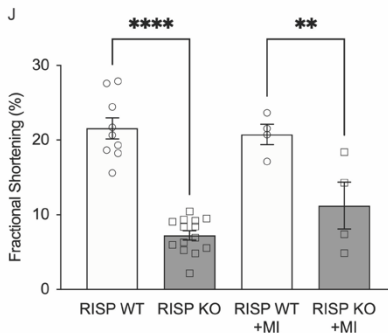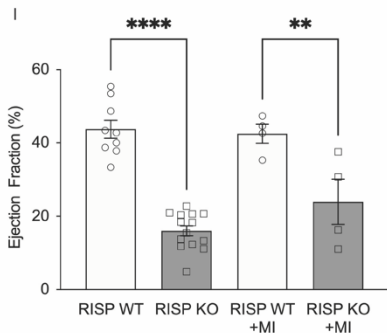1198   ****p<0.0001.

1199

1200

1201

1202

1203

1206

1207

1208   **Figure 5**. New cardiomyocytes in RISP KO infiltrate regions of ischemic damage after

1209   myocardial infarction (MI). The left anterior descending coronary artery was

1210   permanently ligated 45 days post-tamoxifen thus creating a MI in the LV. At 60 days the

1211   hearts were harvested, fixed, and serial-sliced from apex to base. (**A, D**) Representative

1212   H&E-stained heart slices illustrating the MI-induced scar regions in the LV of RISP WT

1213   and KO mice, respectively. Scale bars: 500μm. (**B, E**) Insets of (A) and (D),

1214   respectively. ImageJ was used to trace the boundary between necrotic tissue and non-

1215   necrotic to appreciate the geometry of the necrotic tissue. Finger-like projections of

1216   dividing cardiomyocytes into the damaged tissue were observed in RISP KO hearts (E)

1217   compared to the RISP WT heart (B). (**C, F**) Representative ellipses generated by

1218   ImageJ designating the best fit ellipse based on the boundaries traced in (B) and (E),

1219   respectively. (**G**) Quantitative analysis of the smoothness of the boundaries designating

1220   the scar tissue calculated by dividing the measured parameters of the ellipses

1221   generated in (C, F) by the measured parameters traced in (B, E), respectively.

1222   Boundaries traced in RISP KO hearts were significantly rougher with more finger-like

1223   projections of dividing cardiomyocytes migrating into the injured region compared to WT

1224   hearts. Injured regions were traced in 6-8 heart slices/mouse with n=4 mice per

1225   condition, mean±SEM, U-2t-T-test. (**H**) HW/BW of mice in MI studies demonstrated that

1226   MI did not affect hyperplastic remodeling induced by RISP KO, n=4 mice per conditions,

1227   mean±SEM, U-2t-T-test. (**I**) Differences in LV ejection fraction between RISP WT and

1228   RISP KO mice were unaffected by the MI, compared with WT, n=4-14 mice per

1229   condition, mean±SEM, U-2t-T-test. (**J**) Differences in LV fractional shortening between

1230   RISP WT and KO mice were unaffected by the MI, n=4-14 mice per condition,

1231   mean±SEM, U-2t-T-test.   **p<0.01, ****p<0.0001.

1232
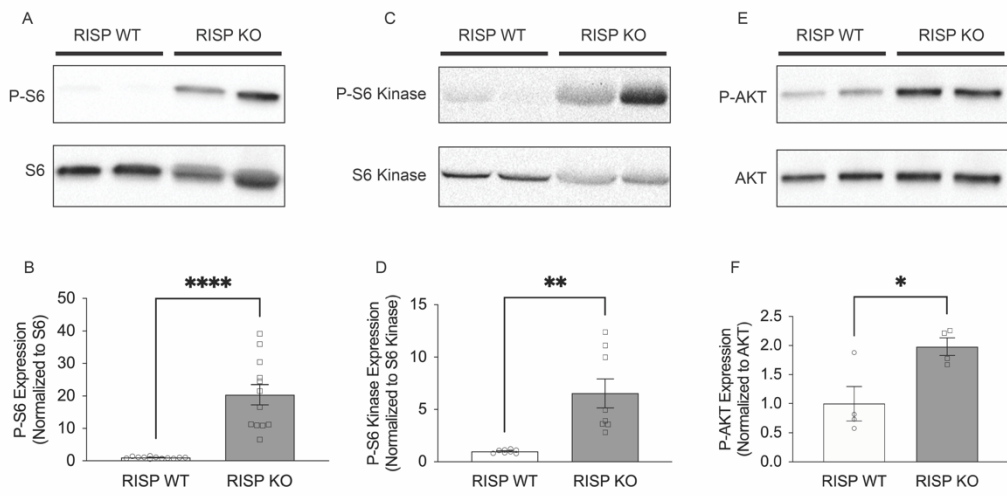
1233

1234

1235 **Figure 6**. mTOR phosphorylation of protein targets is consistent with the observation of

1236 proliferating cardiomyocytes. (**A**) Representative immunoblots of phosphorylated

1237 ribosomal S6 and ribosomal S6 from snap frozen heart homogenates from RISP WT

1238 and KO mice at 60 days post-tamoxifen. (**B**) Band density analysis of phosphorylated

1239 ribosomal S6 and ribosomal S6 from RISP WT and KO mice at 60 days post-tamoxifen,

1240 n=12 mice per condition, mean±SEM, U-2t-T-test. (**C**) Representative immunoblots of

1241 phosphorylated S6 kinase and S6 kinase from RISP WT and KO mice at 60 days post-

1242 tamoxifen. (**D**) Band density analysis of phosphorylated S6 kinase and S6 kinase from

1243 RISP WT and KO mice at 60 days post-tamoxifen, n=8 mice per condition, mean±SEM,

1244 U-2t-T-test. (**E**) Representative immunoblots of phosphorylated (pAkt) and total Akt from

1245 RISP WT and KO mice at 60 days post-tamoxifen. (**F**) Band density analysis of pAkt

1246 and total Akt from RISP WT and KO mice at 60 days post-tamoxifen, n=4 mice per

1247 condition, mean±SEM, U-2t-T-test. *$p<0.05$, **$p<0.01$, ****$p<0.0001$.

1248

1249
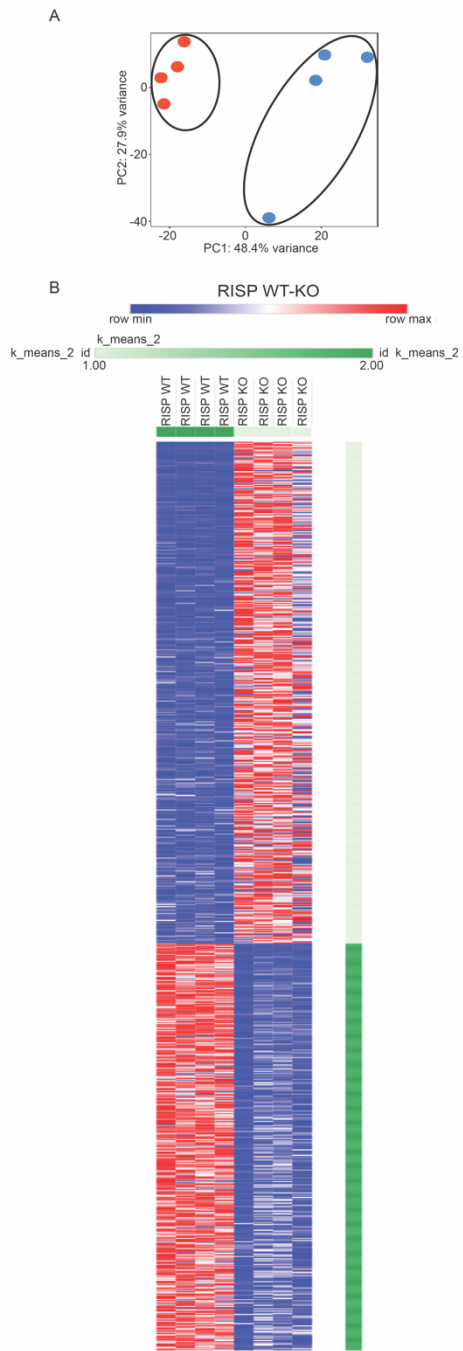
1252 **Figure 7**. Transcriptomic responses in RISP WT and KO hearts at 60 days post-

1253 tamoxifen. (**A**) Principal component analysis of RNA-seq data from RISP WT and KO

1254 hearts. (**B**) K-means 2 clustering of gene expression values for 1355 differentially

1255 expressed genes in RISP WT (n=4 mice, left columns) and KO (n=4 mice, right

1256 columns) (adjusted $p<0.05$, EdgeR-analysis) (red: increased expression relative to

1257 blue).

1258

1259
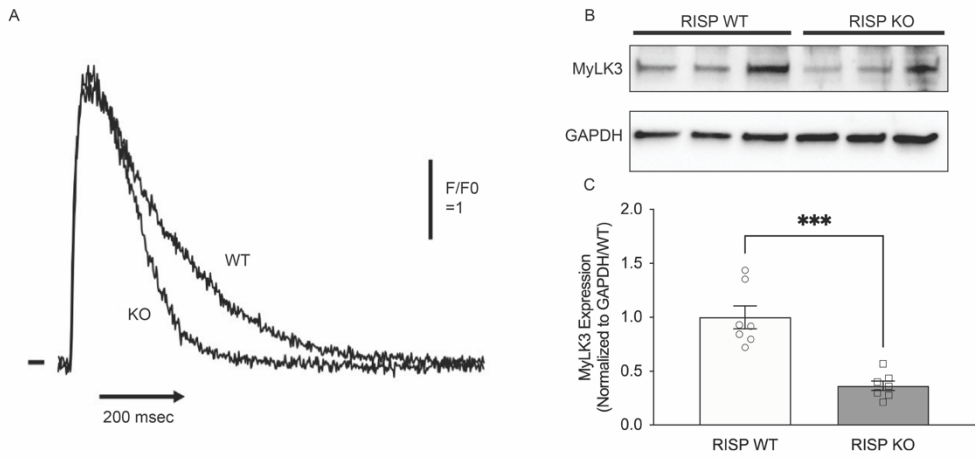
1262   **Figure 8**. (**A**) Ca^{2+} measurements in paced cardiomyocytes revealed that the initial rise

1263   in Ca^{2+} was indistinguishable between RISP WT and KO mice. However, sequestration

1264   of Ca^{2+} was faster in the KO cardiomyocytes compared to WT. Further analysis of Ca^{2+}

1265   dynamics is presented in Supplementary figure S9A-H. (**B**) Immunoblotting for MyLK3

1266   protein revealed a decrease in RISP KO compared to WT hearts at 60 days post-

1267   tamoxifen (**C**) Band density analysis of immunoblots of MyLK3 and GAPDH in RISP WT

1268   and KO hearts at 60 post-tamoxifen, n=7 mice per condition, mean±SEM, U-2t-T-test.

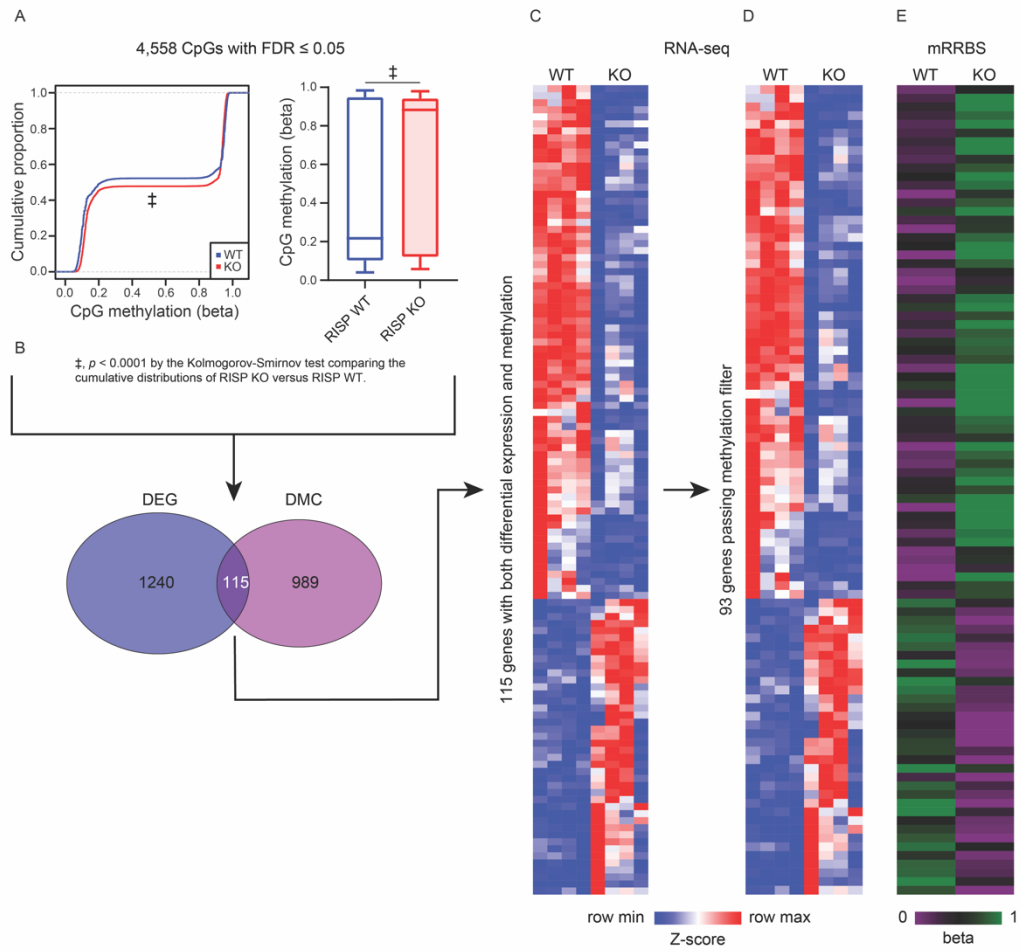1269   ***$p<0.001$.

1270

1271

1272
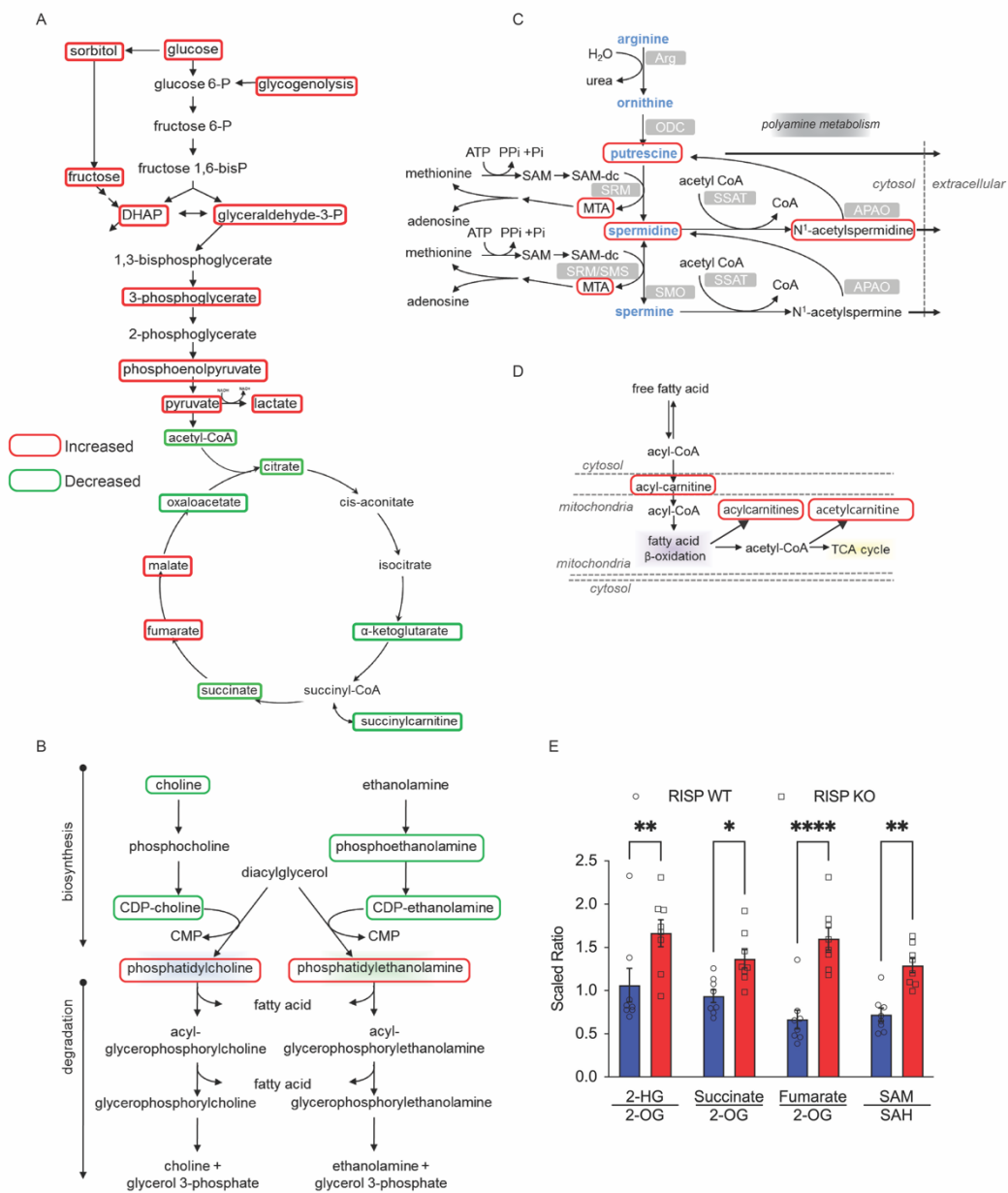
1275 **Figure 9.** Metabolomic responses in RISP WT and KO hearts at 60 days post-

1276 tamoxifen. (**A**) Analysis of glycolytic and TCA cycle biomolecules revealed significant

1277 increases in glycolytic intermediates (red) and decreased abundance of TCA cycle

1278 components (green) in RISP KO, compared to WT hearts ($p < 0.05$. 2t-W-ts-T-test). (**B**)

1279 Analysis of biomolecules involved in membrane synthesis revealed increases in

1280 phosphatidylcholine and phosphatidylenthaolamine (red), along with decreases in

1281 substrates feeding into their synthesis (green) in RISP KO, compared to WT hearts

1282 ($p < 0.05$, 2t-W-ts-T-test). (**C**) Analysis of polyamines revealed increases in putrescine,

1283 spermidine, MTA and N-acytylspermidine (red) in RISP KO, compared to WT hearts

1284 ($p < 0.05$, 2t-W-ts-T-test). (**D**) Analysis of fatty acid oxidation intermediates revealed

1285 increases in acyl-carnitines (red) in RISP KO, compared to WT hearts ($p < 0.05$, 2t-W-ts-

1286 T-test). (**E**) Scaled ratio of biochemical factors that promote DNA methylation in RISP

1287 WT (blue) and KO hearts (red), n=8 mice per condition, mean±SEM, U-2t-T-test.

1288 *$p < 0.05$, **$p < 0.01$, ****$p < 0.0001$.

1289

1290
1291

A

4,558 CpGs with FDR ≤ 0.05

‡, *p* < 0.0001 by the Kolmogorov-Smirnov test comparing the cumulative distributions of RISP KO versus RISP WT.

C   RNA-seq

D

E   mRRBS

115 genes with both differential expression and methylation

93 genes passing methylation filter

1292

1293

1294 **Figure 10.** Epigenetic analysis of RISP WT and KO hearts. (**A**) Left: Cumulative

1295 distribution of DNA CpG methylation in RISP WT (blue) and KO (red) hearts. Right:

1296 Box-whisker plot showing significant increase in DNA CpG methylation (DMC) in RISP

1297 KO compared with WT hearts ($p<0.0001$, Kolmogorov-Smirnov test). (**B**) Venn diagram

1298 comparing differentially expressed genes (DEG) and differentially methylated DNA CpG

1299 sites located in regulatory regions of genes, reveals an overlap of 115 genes. (**C**) K-

1300 means clustering of RNA-seq identification of 115 DEG and DMC genes showing

1301 directional change (up- (red) vs. down- (blue) regulated) in RISP KO (n=4) versus WT

1302 hearts (n=4). (**D**) K-means clustering after filtering was applied to restrict the dataset to

1303 CpGs with 25% higher methylation in lower expression groups compared with higher

1304 expression groups; this identified 93 DEG and DMC genes in RISP KO (n=4) versus WT

1305 hearts. (**E**) DNA CpG methylation status of 93 DMC and DEG showing that down-

1306 regulated genes are more highly methylated (green) in regulatory regions, while up-

1307 regulated genes are less highly methylated (violet), in RISP KO compared with WT. For

1308 panels C-E, DEG were determined using a generalized linear model and ANOVA-like

1309 testing with FDR q-value < 0.05, and DMC were determined using a beta-binomial

1310 regression model with an arcsine link function fitted using the generalized least square

1311 method and Wald-test FDR q-value < 0.05.

1312

1313